



Reynolds number effects on turbulent flow in curved channels

Giulio Soldati¹ , Paolo Orlandi¹  and Sergio Pirozzoli¹ 

¹Dipartimento di Ingegneria Meccanica e Aerospaziale, Sapienza Università di Roma, via Eudossiana 18, Roma, Italy

Corresponding author: Giulio Soldati, giulio.soldati@uniroma1.it

(Received 12 September 2024; revised 20 December 2024; accepted 2 January 2025)

We investigate fully developed turbulent flow in curved channels to explore the interaction between turbulence and curvature-driven coherent structures. By focusing on two cases of mild and strong curvature, we examine systematically the effects of the Reynolds number through a campaign of direct numerical simulations, spanning flow regimes from laminar up to the moderately high Reynolds number – based on bulk velocity and channel height – of 87 000. Our analysis highlights the influence of curvature on the friction coefficient, showing that flow transition is anticipated by concave curvature and delayed by convex curvature. In the case of mild curvature, a frictional drag reduction compared with plane channel flow is found in the transitional regime. Spectral analysis reveals that the near-wall turbulence regeneration cycle is maintained in mildly curved channels, while it is absent or severely inhibited on the convex wall of strongly curved channels. Streamwise large-scale structures resembling Dean vortices are found to be weakly dependent on the Reynolds number and strongly affected by curvature: increasing curvature shifts these vortices towards the outer wall and reduces their size and coherence, limiting their contribution to streamwise velocity fluctuations and momentum transport. In the case of strong curvature, spanwise large-scale structures are also detected. These structures are associated with large pressure fluctuations and the suppression of turbulent stresses near the convex wall, where a region with negative turbulence production is observed and characterised via quadrant analysis.

Key words: turbulence simulation

1. Introduction

Turbulence bounded by curved walls is a key aspect of various engineering applications, such as highly cambered aerofoils, turbo-machinery blades and cooling channels. In these configurations, curvature alters significantly the turbulence structures, impacting friction, heat transfer and flow stability. The spatially evolving and geometry-dependent nature of these flows poses major challenges in developing a unified and comprehensive description of curvature effects on turbulence, which can be achieved by considering the time-evolving curved channel flow. Direct numerical simulations (DNS) of plane channel flow led to a scientific breakthrough in the theory of wall-bounded turbulence through the pioneering work of Kim, Moin & Moser (1987), and subsequent efforts at higher Reynolds numbers were made by Lee & Moser (2015) and by Pirozzoli *et al.* (2021) for the circular pipe flow. In a similar vein, we scrutinise the effect of the Reynolds number on flow in curved channels, with the aim of providing a benchmark dataset for Reynolds-averaged Navier–Stokes (RANS) and large-eddy simulations (LES) of turbulent flows over curved surfaces.

Compared with flat walls, surface curvature produces additional strain rates an order of magnitude larger than what dimensional arguments would suggest (Bradshaw & Young 1973). The laminar solution of the equations of motion indicates that the effects of surface curvature (κ) on quantities such as the friction coefficient and boundary layer thickness (δ) are of the order $O(\kappa\delta)$. However, experimental measurements in turbulent flow reveal much stronger effects, underscoring the direct impact of curvature on turbulence. Rayleigh (1917) first investigated the stability of inviscid disturbances in curved channel flow around its laminar solution, deducing flow stability as a balance between the centrifugal force per unit mass ($\rho U^2/r$, where U is the streamwise velocity at distance r from the centre of curvature) and the radial pressure gradient ($\partial P/\partial r$). Specifically, he found that for flow over a concave surface the centrifugal force of the displaced fluid element is greater than the centripetal pressure gradient, leading to flow instability, whereas the reverse occurs for convex walls. This idea is known as ‘Rayleigh’s criterion for centrifugal instability’, and was later supported by experimental evidence (Wattendorf 1935; Eskinazi & Yeh 1956; Ellis & Joubert 1974). Using the narrow-gap approximation, Dean (1928) showed analytically that fully developed flow between two concentric cylinders becomes centrifugally unstable when the Reynolds number exceeds a critical value, which decreases as the channel curvature increases. When the instability sets in, large-scale secondary motions are generated in the form of streamwise-aligned counter-rotating vortices, commonly referred to as Dean vortices. Due to these flow structures, a downwash (upwash) motion is generated between a vortex pair, resulting in a corresponding peak (trough) in the friction coefficient. Footprints of large-scale streamwise-aligned vortices were found also in the turbulent regime: experiments on curved duct flow (Brewster, Grosberg & Nissan 1959; Ellis & Joubert 1974; Hunt & Joubert 1979) highlighted regular spanwise variations in mean velocity and friction coefficient, which were considered evidence for the existence of Dean vortices-like structures. Other experiments (Eskinazi & Yeh 1956; Ramaprian & Shivaprasad 1978; Kobayashi *et al.* 1989), however, did not detect any spanwise variation.

The dynamics of streamwise vortices may be unsteady due to events of splitting and merging, depending on channel curvature and Reynolds number. Through experiments in a curved duct, Ligrani & Niver (1988) and Ligrani *et al.* (1994) observed the splitting of vortex pairs, during which new vortices seem to emerge from the concave wall between existing pairs. Splitting and merging phenomena were also detected by Alfredsson &

Persson (1989) in channels with spanwise rotation and by Matsson & Alfredsson (1990) in a channel with both curvature and rotation. The origin of this phenomenon was investigated by Guo & Finlay (1991) who found that vortex splitting and merging in curved channels are caused by Eckhaus instability, namely a secondary instability of steady periodic flows (such as the Dean vortex flow) with respect to spanwise perturbations (Eckhaus 1965).

Flow in curved channels is further complicated by secondary instabilities with respect to streamwise perturbations. In fact, in numerical simulations of curved channels with roll cells, Finlay, Keller & Ferziger (1988) observed a ‘wavy Dean vortex flow’ in the form of travelling waves superposed on the secondary flow (the Dean vortices). Those authors suggested that travelling waves are originated by a shear-layer instability induced by the Dean vortices. Consistently, the stability analysis carried out by Yu & Liu (1991) identified the inflectional profile of the mean velocity as the mechanism driving the secondary instability. The same secondary instability was found also experimentally by Matsson & Alfredsson (1990), who described it as a ‘wave train riding on the primary instability’ (Matsson & Alfredsson 1992).

The distinctive three-dimensional effects associated with concave curvature are absent in the case of convex curvature, whose main effect is to reduce turbulence intensity (Gillis & Johnston 1983). Indeed, So & Mellor (1973) found experimentally that the turbulent stress decreases near the wall and vanishes approximately midway between the convex surface and the edge of the velocity gradient layer. The reduction in turbulent shear stress due to convex curvature leads to a shift of the zero-crossing point closer to the convex wall. This asymmetry is associated with a displacement between the locations where turbulent and viscous shear stresses vanish, giving rise to a region with negative production of turbulent kinetic energy (TKE). This phenomenon was examined by Eskinazi & Erian (1969), who related it to a local ‘energy reversal mechanism’, whereby energy is transferred from turbulent fluctuations to the mean flow.

Despite the large amount of laboratory data available in the literature, the effects of curvature on turbulence have neither been fully quantified nor understood. Due to the narrow range of both Reynolds numbers and curvatures spanned by the experiments conducted so far, it is difficult to draw general conclusions. Additionally, it is often unclear whether the flow is fully developed, inflow conditions are free of disturbances and three-dimensional effects due to sidewalls are negligible. The obvious candidate to understand the flow physics in greater detail is DNS. The first major contribution from DNS was made by Moser & Moin (1987), who studied fully developed turbulent flow at bulk Reynolds number $Re_b = u_b \delta / \nu = 5200$ (where u_b is the bulk velocity, δ the channel height and ν the kinematic viscosity) in a curved channel with curvature radius $r_c / \delta = 39.5$ at the channel centreline. They concluded that most turbulence quantities, except for the turbulent shear stress, are equivalent on the convex and concave sides of the channel when scaled in local wall units, inferring the existence of flow similarity. However, Nagata & Kasagi (2004), who carried out several DNS of mildly ($r_c / \delta = 39.5$) to moderately ($r_c / \delta = 2.5$) curved channel flow at $Re_b \approx 4600$, did not observe near-wall similarity, especially for the strongest curvature considered. Contrary to previous studies, they suggested that large-scale roll cells primarily contribute to turbulence production near the convex wall, rather than the concave wall. Ambiguities in assessing the effects of large-scale structures may arise from the use of periodicity conditions in the streamwise direction combined with short computational domains, artificially enhancing their coherence. In addition, narrow domains in the spanwise direction can constrain the wavelength of Dean-like vortices. These issues were addressed by Brethouwer (2022), who employed DNS to investigate fully developed turbulent flow in channels with mild ($r_c / \delta = 30$) to moderate ($r_c / \delta = 3$)

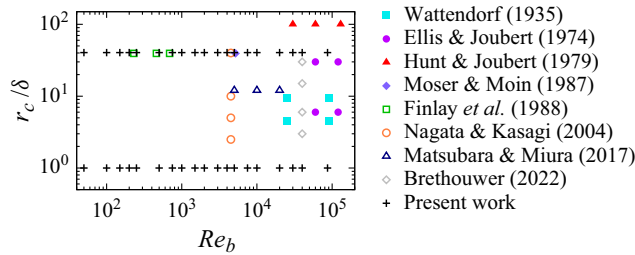


Figure 1. Overview of previous experimental and computational studies of curved channel flow in terms of bulk Reynolds number (Re_b), and relative curvature radius (r_c/δ). Crosses indicate the flow cases computed in the present work.

curvature using significantly larger domains. The Reynolds number was increased to $Re_b = 40\,000$, ensuring clear separation between near-wall turbulence scales and large-scale streamwise vortices. Based on this improved set-up, velocity fluctuations in local scaling turned out to collapse into a single curve in the viscous wall region, whereas they were found to depend heavily on curvature in the outer layer. The contribution of large-scale streamwise vortices to turbulence production was found to be substantial for all curvatures considered, especially near the concave wall. Despite accurate data and valuable insights on curvature effects on turbulence, that study was restricted to a single Reynolds number and did not cover the case of strong wall curvature.

Given this background, in this work we aim to extend our understanding of turbulence in curved channels by widening the range of Reynolds numbers and examining cases with extreme curvature, thus filling existing gaps in the current literature. This is well illustrated in [figure 1](#), which reports an overview of the controlling flow parameters, namely bulk Reynolds number (Re_b) and relative curvature radius (r_c/δ), from previous experimental and computational studies of curved channel flow, along with our DNS. We investigate the effects of channel curvature by focusing on two extreme cases, namely a mildly ($r_c/\delta = 40.5$) and strongly ($r_c/\delta = 1$) curved channel. According to the definition proposed by Hunt & Joubert (1979), these two cases correspond to ‘shear-dominated’ and ‘inertia-dominated’ flows, respectively. For both cases, we examine the effect of the Reynolds number – which has never been studied systematically for this flow configuration – by carrying out a DNS campaign covering a wide range of flow regimes. Special attention is paid to friction, specifically to how the changes in flow organisation and turbulence structures induced by curvature affect its behaviour. This analysis reveals important insights into the flow transition, which varies according to the type and magnitude of curvature. In addition, we focus on characterising the secondary motions induced by large-scale structures that develop in curved channel flow.

The paper is structured as follows: in § 2 we describe the numerical methodology used for the analysis; in § 3 we present the main results of the DNS campaign, specifically, the friction coefficient and flow transition are studied in § 3.1; the flow organisation is explored through instantaneous velocity fields in § 3.2 and time-averaged velocity spectra in § 3.3; streamwise large-scale structures are addressed in § 3.4, with a focus on splitting and merging events in § 3.5, and on their role on velocity fluctuations in § 3.6; spanwise large-scale structures are discussed in § 3.7, and their role on shear stress and pressure fluctuations at the convex wall is analysed in § 3.8; the structure of the turbulent shear stress is investigated in § 3.9 through a quadrant analysis, and a region with negative production is observed and examined in § 3.10; finally, in § 4 we conclude with a discussion of the results.

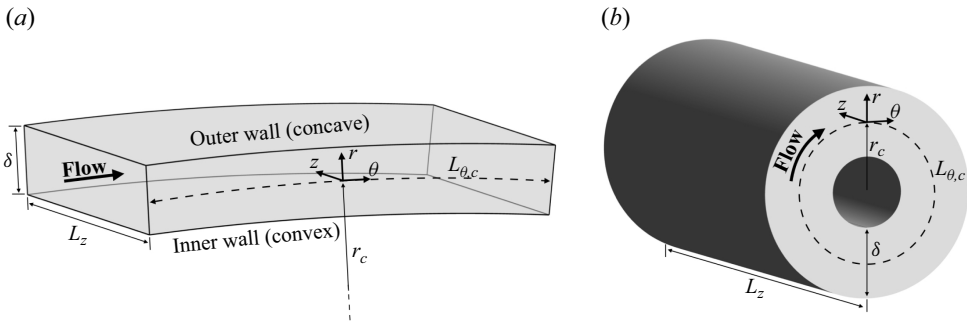


Figure 2. Computational set-up for flow in mildly (a) and strongly (b) curved channels.

2. Methodology

The turbulent flow in curved channels is simulated in a computational domain bounded by sectors of concentric cylinders, as shown in figure 2. The velocity components along the streamwise (θ), radial (r) and spanwise (z) directions are denoted by u , v and w , respectively. The flow is driven by a mean-pressure gradient ($\partial P/\partial\theta$), which is imposed as a volumetric forcing to maintain constant mass flow rate in time. Numerical simulations are carried out assuming periodicity conditions in the streamwise and spanwise directions, so that the flow is fully developed.

The in-house code used for DNS, which solves the incompressible Navier–Stokes equations in cylindrical coordinates, stems from a previous solver developed by Verzicco & Orlandi (1996) and used for DNS of pipe flow by Orlandi & Fatica (1997). The switch from the pipe set-up to the curved channel was attained by implementing two main modifications to the code. The first is the addition of an inner cylinder (the inner wall of the channel) concentric to the outer cylinder. The second is the change in direction of the mean-pressure gradient, which is imposed along the azimuthal direction (θ), namely the streamwise direction of the curved channel. In this respect, we note that the pressure term in the streamwise momentum equation is $(\partial P/\partial\theta)/r$, with constant $\partial P/\partial\theta$, hence the volumetric forcing varies along the radial direction. The spatial discretisation is based on second-order finite-difference schemes, which are implemented in the classical marker-and-cell framework (Harlow & Welch 1965). The pressure is located at the cell centres, whereas the velocity components are at the cell faces, thus removing odd–even decoupling phenomena and guaranteeing discrete conservation of the total kinetic energy in the inviscid limit (Pirozzoli 2023). The governing equations are advanced in time by means of a hybrid third-order low-storage Runge–Kutta algorithm, whereby the diffusive terms are handled implicitly and the convective terms explicitly. Further details regarding the numerical methods implemented in the code can be found for example in Pirozzoli *et al.* (2021). The code was adapted to run on clusters of graphic accelerators (GPUs), using a combination of CUDA Fortran and OpenACC directives, and relying on the CUDA libraries for efficient execution of fast Fourier transforms.

The flow field is controlled by two parameters, namely the bulk Reynolds number, Re_b , and the radius of curvature at the centreline, r_c/δ . To investigate the effect of both parameters, we split the simulation campaign in two main groups: (i) shear-dominated flow with mild curvature ($r_c/\delta = 40.5$), and (ii) inertia-dominated flow with strong curvature ($r_c/\delta = 1$). Throughout the paper, we will refer to the first group as R40 and to the second group as R1. Within each group, we vary the Reynolds number from $Re_b = 25$ up to 87 000. The domain extends in the radial direction from $r = r_i$ (inner wall), to $r = r_o$ (outer

wall), where $r_o - r_i = \delta$ and $r_c = (r_i + r_o)/2$. To compare cases with different values of the curvature radius, we consider the y -coordinate, aligned with the radial direction and origin shifted at the inner wall, i.e. $y = y_i = r - r_i$. In all cases, the computational domain has a streamwise length $L_\theta/\delta = 2\pi$ along the centreline, meaning that for the R1 cases the domain covers a full circumference (see [figure 2](#)). The spanwise width is set to $L_z/\delta = 4$ for the R40 cases, and it is doubled for R1 cases, in order to minimise the influence of spanwise periodicity on the large-scale structures. The effects of the domain sizes on the simulations results are assessed in [appendix A](#). Domain sizes, number of grid points and grid spacings are listed in [table 1](#), along with the resulting friction Reynolds number at the inner ($Re_{\tau,i} = u_{\tau,i}\delta/2\nu$) and outer wall ($Re_{\tau,o} = u_{\tau,o}\delta/2\nu$). Distinction between the inner and outer wall is necessary as the friction velocity changes depending on the wall at which it is evaluated. A global friction velocity can also be defined based on the mean-pressure gradient, as shown in previous works (e.g. Moser & Moin 1987; Brethouwer 2022). Inner, outer and global friction velocities are defined, respectively, as

$$u_{\tau,i} = \sqrt{\nu \frac{\partial U}{\partial r} \Big|_{r_i}}, \quad u_{\tau,o} = \sqrt{\nu \frac{\partial U}{\partial r} \Big|_{r_o}}, \quad u_{\tau,g} = \sqrt{\frac{u_{\tau,i}^2 r_i^2 + u_{\tau,o}^2 r_o^2}{2r_c^2}}, \quad (2.1)$$

where $u_{\tau,g}$ is derived in [appendix B](#).

Throughout the paper, we will use two types of normalisation: local wall scaling, based on $u_{\tau,i}$ and $u_{\tau,o}$ (denoted with the ‘plus’ superscript), and global wall scaling, based on $u_{\tau,g}$ (denoted with the ‘star’ superscript). Capital letters denote flow properties averaged in the homogeneous spatial directions and in time, and lower-case letters denote instantaneous values. Hence, $u = U + u'$, where u' is the fluctuation from the mean. Brackets denote the averaging operator (with subscripts indicating the space coordinates over which averaging is done) and the overline is reserved for temporal averages, namely $\bar{u} = \frac{1}{T} \int_{t_1}^{t_2} u dt$, where the averaging period is $T = t_2 - t_1$. The grid spacings in local wall scaling ($r_o^+ \Delta\theta$ and Δr_o^+) listed in [table 1](#) are evaluated at the outer wall, which is the most critical as the wall shear stress is higher and the grid spacing in the streamwise direction is larger. All simulations are run up to $t_1 = 600\delta/u_b$, sufficient to reach a statistically steady state, and further for $T = 600\delta/u_b$ to ensure convergence of statistics, which is verified in [appendix C](#).

3. Results

3.1. Friction coefficient and flow transition

The friction coefficient is a key parameter for characterising the transition from laminar to turbulent flow in curved channels. According to the various definitions of friction velocity given in (2.1), we define local friction coefficients at the inner and at the outer wall, as well as a global friction coefficient,

$$C_{f,i} = 2 \left(\frac{u_{\tau,i}}{u_b} \right)^2, \quad C_{f,o} = 2 \left(\frac{u_{\tau,o}}{u_b} \right)^2, \quad C_{f,g} = 2 \left(\frac{u_{\tau,g}}{u_b} \right)^2, \quad (3.1)$$

shown in [figure 3](#) as a function of the bulk Reynolds number. The global friction (in the inset) is related to the mean-pressure gradient (B3), hence to the power expenditure to drive the flow. For comparison with the plane channel, we also report the friction law for laminar flow, $C_f = 12/Re_b$ (dashed line in the inset), and the logarithmic friction relation,

Mild curvature (R40): $r_c/\delta = 40.5, L_\theta/\delta \times L_z/\delta = 2\pi \times 4$				
Re_b	$Re_{\tau,i}$	$Re_{\tau,o}$	$N_\theta \times N_r \times N_z$	$r_o^+ \Delta\theta \times \Delta r^+ \times \Delta z^+$
25	6	6	129 × 65 × 129	0.6 × 0.01 × 0.4
50	9	9	129 × 65 × 129	0.9 × 0.01 × 0.5
100	12	12	129 × 65 × 129	1.2 × 0.01 × 0.8
150	15	15	129 × 65 × 129	1.5 × 0.01 × 0.9
200	17	17	129 × 65 × 129	1.7 × 0.01 × 1.0
250	19	19	129 × 65 × 129	1.9 × 0.01 × 1.2
500	28	31	129 × 65 × 129	3.1 × 0.01 × 2.0
750	35	40	129 × 65 × 129	4.0 × 0.02 × 2.5
1000	41	50	129 × 65 × 129	5.0 × 0.01 × 3.1
1500	51	65	161 × 97 × 161	5.2 × 0.01 × 3.2
2000	61	78	193 × 97 × 193	5.2 × 0.01 × 3.3
2500	69	92	225 × 97 × 225	5.3 × 0.02 × 3.3
3000	82	112	257 × 129 × 257	5.6 × 0.01 × 3.5
4000	103	143	321 × 129 × 321	5.8 × 0.01 × 3.6
5000	139	170	321 × 145 × 353	6.8 × 0.01 × 3.8
7500	211	241	449 × 145 × 449	6.9 × 0.02 × 4.3
10 000	270	305	513 × 161 × 513	7.7 × 0.02 × 4.8
20 000	506	583	769 × 205 × 1025	9.8 × 0.03 × 4.6
30 000	720	839	1153 × 261 × 1537	9.4 × 0.03 × 4.4
40 000	922	1085	1409 × 303 × 1793	9.9 × 0.03 × 4.8
87 000	1824	2177	3073 × 489 × 3585	9.1 × 0.03 × 4.8
Strong curvature (R1): $r_c/\delta = 1.0, L_\theta/\delta \times L_z/\delta = 2\pi \times 8$				
Re_b	$Re_{\tau,i}$	$Re_{\tau,o}$	$N_\theta \times N_r \times N_z$	$r_o^+ \Delta\theta \times \Delta r^+ \times \Delta z^+$
25	8	5	129 × 65 × 129	0.8 × 0.01 × 0.7
50	11	8	129 × 65 × 129	1.1 × 0.01 × 1.0
75	14	10	129 × 65 × 129	1.5 × 0.01 × 1.3
100	16	12	129 × 65 × 129	1.8 × 0.01 × 1.5
150	20	15	129 × 65 × 129	2.2 × 0.01 × 1.9
200	23	18	129 × 65 × 129	2.6 × 0.01 × 2.2
250	26	21	129 × 65 × 129	3.0 × 0.01 × 2.6
500	39	35	129 × 65 × 129	5.1 × 0.01 × 4.4
750	49	47	161 × 65 × 193	5.5 × 0.02 × 3.9
1000	58	58	193 × 97 × 257	5.7 × 0.01 × 3.6
1500	73	79	225 × 97 × 289	6.7 × 0.01 × 4.4
2000	86	98	225 × 129 × 385	8.2 × 0.01 × 4.0
2500	98	115	289 × 129 × 449	7.6 × 0.01 × 4.1
3000	110	132	385 × 129 × 513	6.5 × 0.01 × 4.1
4000	132	165	449 × 145 × 513	6.9 × 0.01 × 5.1
5000	152	193	449 × 145 × 769	8.1 × 0.02 × 4.0
7500	199	263	577 × 145 × 961	8.6 × 0.02 × 4.4
10 000	244	327	641 × 161 × 1153	9.6 × 0.04 × 4.5
20 000	403	563	1153 × 205 × 2049	9.2 × 0.03 × 4.4
30 000	551	784	1665 × 261 × 2817	8.8 × 0.02 × 4.4
40 000	697	995	2049 × 303 × 3585	9.2 × 0.02 × 4.4
87 000	1362	1952	4097 × 489 × 7169	9.0 × 0.02 × 4.4

Table 1. Flow parameters for DNS: bulk Reynolds number, friction Reynolds number at the inner and outer wall, number of grid points and grid spacing in inner units in the streamwise, radial and spanwise directions, respectively. The title line reports curvature radius and domain extension in the streamwise (along the centreline) and spanwise directions.

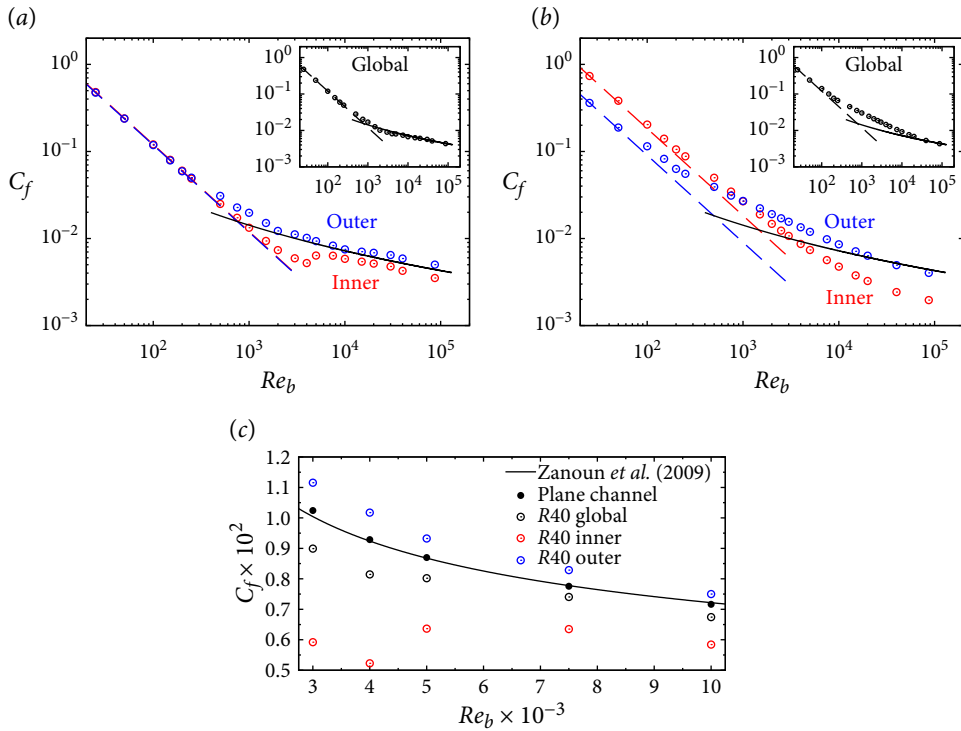


Figure 3. Friction coefficient as a function of the bulk Reynolds number for the R40 flow cases (a) and R1 flow cases (b). Red circles denote the local friction coefficient at the inner wall ($C_{f,i}$), blue circles at the outer wall ($C_{f,o}$), black circles in the insets denote the global friction coefficient ($C_{f,g}$); dashed lines denote the analytical friction law for laminar flow (red for the convex wall, blue for the concave wall, black for the plane channel), black solid lines the logarithmic friction relation for plane channel flow (3.2). A magnified view of the friction trend for the R40 flow cases is shown in panel (c).

$$\sqrt{\frac{2}{C_f}} = \frac{1}{k} \left[\ln \left(\frac{Re_b}{2} \sqrt{\frac{C_f}{2}} \right) - 1 \right] + A \tag{3.2}$$

(solid line), obtained by Zanoun, Nagib & Durst (2009) from the logarithmic law of the wall, with log-law constants $k = 0.41$, $A = 5.17$.

In the turbulent regime, the friction at the outer wall is consistently higher than at the inner wall due to increased turbulence intensity. For the R40 flow cases (figure 3a), the friction coefficient of a plane channel at the same flow rate (black solid line) lies approximately midway between the values at the two walls of the curved channel and is comparable to the global friction. In contrast, for the R1 flow cases (figure 3b), the inner-wall friction is significantly lower than that of an equivalent plane channel. However, the global friction is higher and aligns with the plane channel only for $Re_b \geq 40\,000$.

To comment more clearly on the friction trend in the laminar and transitional regime, it is useful to consider the mean velocity profiles at representative Reynolds numbers, as reported in figure 4. At low Reynolds number, the flow in a curved channel is laminar and the velocity profile can be derived analytically as

$$U(r) = \alpha r - \frac{\beta}{r} - r \ln r, \tag{3.3}$$

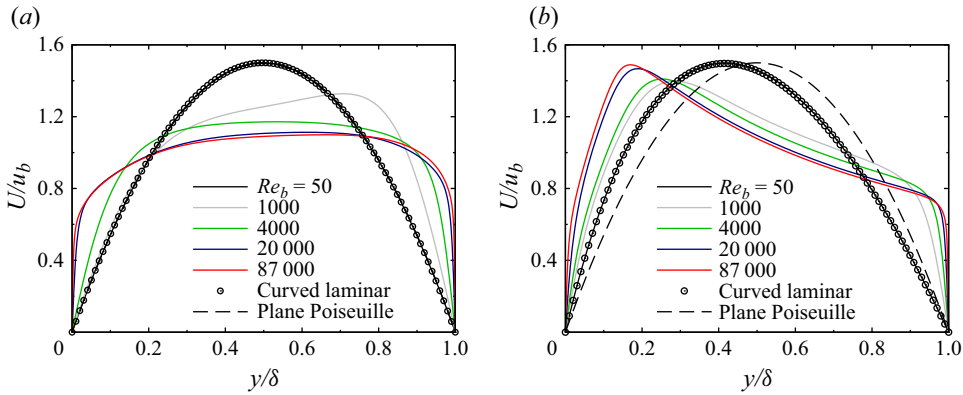


Figure 4. Mean streamwise velocity (U/u_b) at various Reynolds numbers for the R40 flow cases (a) and R1 flow cases (b). Black dashed lines refer to the Poiseuille profile, black circles to the velocity profile for laminar curved channel flow (3.3).

where

$$\alpha = \frac{r_o^2 \ln r_o - r_i^2 \ln r_i}{r_o^2 - r_i^2}, \quad \beta = \frac{r_i^2 r_o^2 \ln(r_o/r_i)}{r_o^2 - r_i^2}. \quad (3.4)$$

In the R40 flow cases, the laminar velocity profile is nearly identical to the parabolic profile of plane channel flow, meaning that the shear stress distribution is almost symmetrical. As the curvature increases, the pressure gradient in the radial direction becomes stronger and the location of maximum velocity shifts towards the inner wall. As a result, the shear stress is larger at the inner wall than at the outer wall. In the laminar regime, the friction coefficient at the two walls can be determined analytically from (3.3), thus obtaining

$$\frac{dU(r)}{dr} = \alpha + \frac{\beta}{r^2} - \ln r - 1. \quad (3.5)$$

For the R40 flow cases, we find $C_{f,i} \approx 12.03/Re_b$, hence nearly identical to plane Poiseuille flow, and $C_{f,o} \approx 11.83/Re_b$. In contrast, in the R1 flow cases the friction coefficient at the inner wall, $C_{f,i} \approx 18.34/Re_b$, is approximately twice as at the outer wall, $C_{f,o} \approx 9.04/Re_b$. Flow transition occurs when the Reynolds number attains a critical value at which centrifugal instability sets in and Dean vortices form, similarly to the Taylor vortices in flow between two rotating cylinders (Taylor 1923). Here, the critical Reynolds number is defined as the point where the friction coefficient deviates from the laminar trend by at least 2 %, an amount higher than the uncertainty of time-averaged measurements. For the R40 flow cases the critical Reynolds number is $Re_b \approx 250$, which is in good agreement with the value of 228.5 found by Finlay *et al.* (1988), whereas for the R1 flow cases transition starts earlier, at $Re_b \approx 50$. The transitional regime is greatly affected by curvature, with convex curvature (inner wall) tending to stabilise the flow, and concave curvature (outer wall) having the opposite effect. This is particularly evident in the R40 flow cases: at $Re_b = 1000$, the flow near the inner wall is laminar, as visible from the mean velocity profile in figure 4(a). In contrast, secondary motions are generated near the outer wall, which results in stronger momentum exchange. The peak velocity then shifts towards the outer wall, resulting in higher friction. At $Re_b = 4000$, the flow near the outer wall is fully turbulent (as will be shown later through flow visualisations), whereas the velocity profile near the inner wall remains close to the laminar state. Hence, mild

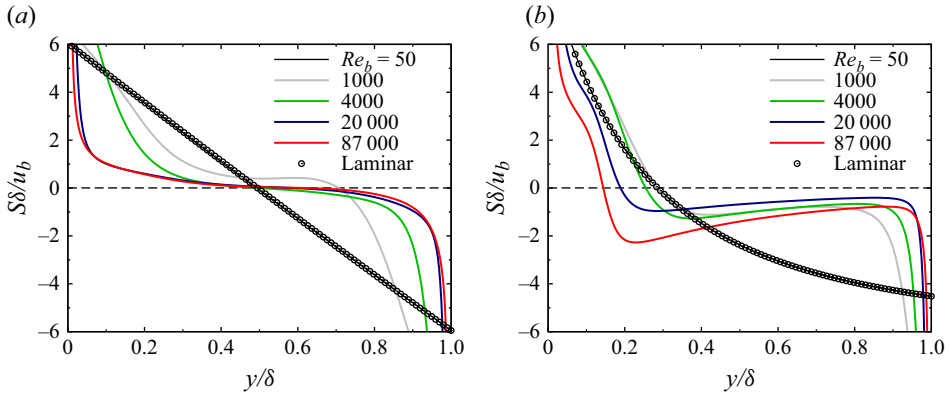


Figure 5. Mean shear rate ($S\delta/u_b$) at various Reynolds numbers for the R40 flow cases (a) and R1 flow cases (b). Circles denote the analytical profile for the laminar case.

convex curvature tends to delay transition, as plane channel flow becomes turbulent at $Re_b \approx 2600$ (Yimprasert *et al.* 2021). Due to this stabilising effect, the transitional flow regime near the inner wall extends well into the range of Reynolds numbers for which fully turbulent flow is expected in plane channels. As a result, the global friction in the range $3000 \leq Re_b \leq 10\,000$ is less than predicted from (3.2), as clearly shown from the magnified view in figure 3(c). This deviation reaches its maximum at $Re_b = 4000$, with a drag reduction of 12.2% with respect to the plane channel data (Orlandi, Bernardini & Pirozzoli 2015). By increasing the Reynolds number to 5000, the flow near the inner wall undergoes abrupt transition to a fully turbulent state, as indicated by the jump in the friction trend indicated by red circles in figure 3(a). This type of transition from laminar to turbulent regime is typical of canonical wall flows (see e.g. Patel & Head 1969), however, it quite different than at the outer wall, where transition is facilitated by centrifugal instabilities and occurs more smoothly.

For the R1 flow cases, friction in the laminar regime is higher at the inner wall. By increasing the Reynolds number, the velocity profiles tend to flatten at the outer wall, where friction increases. Turbulence is inhibited near the inner wall, and friction deviates less markedly from the laminar trend. An inversion occurs past $Re_b \approx 1000$, whereby friction at the outer wall becomes higher than that at the inner wall. Flow transition is facilitated by strong channel curvature, and it occurs smoothly at both walls. At the outer wall, the different transition from canonical wall flows is due to centrifugal (primary) instabilities. As we will show, in the R1 flow cases secondary motions associated with centrifugal instabilities do not reach the inner wall, and transition is affected by streamwise (secondary) instabilities, which lead to the formation of large-scale cross-stream structures.

In figure 5 we show the mean shear rate, $S = dU/dr - U/r$. Similar to the case of the plane channel, the location where the mean shear vanishes can be used to define a bound for the regions of influence of the two walls. In the R40 flow cases (figure 5a) the shear rate profile is nearly symmetrical, hence this location coincides roughly with the channel centreline, with exception of the case $Re_b = 1000$, for which it occurs at $y/\delta \approx 0.71$. In contrast, for the R1 flow cases (figure 5b) the shear rate profile is strongly asymmetrical, the zero crossing shifting towards the inner wall and approaching it as the Reynolds number increases. Hence, the region of influence of the inner wall is much narrower than for the outer wall. In case of strong curvature, the shear rate profile exhibits a local

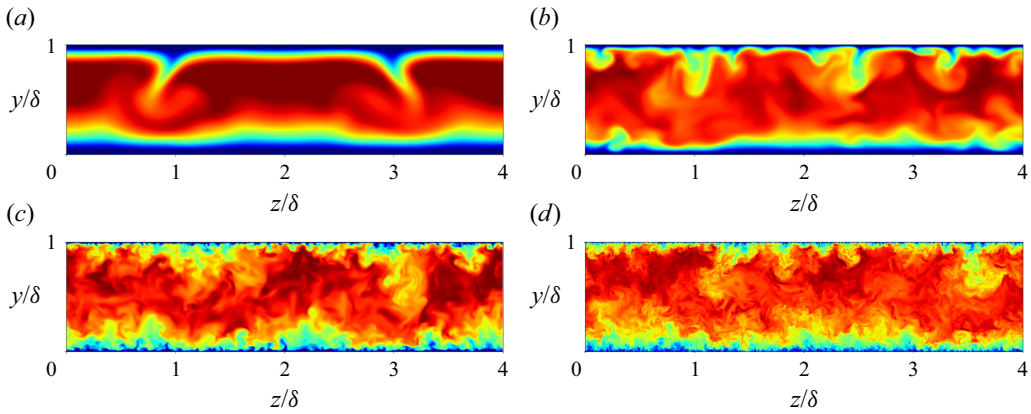


Figure 6. Instantaneous streamwise velocity fields in a cross-stream plane for the R40 flow cases at $Re_b = 1000$ (a), 4000 (b), 20 000 (c), 87 000 (d). The flooded contours range from $0.2 u_b$ (blue) to $1.2 u_b$ (red).

maximum near the outer wall and a local minimum near the inner wall, corresponding to inflectional points of the mean velocity profiles. This showcases the presence of shear layers that can support inflectional instabilities.

3.2. Flow visualisations

The previous discussion on flow transition can be visualised through the instantaneous fields of streamwise velocity in cross-stream and wall-parallel planes, which we show in figures 6 and 7 for the R40 flow cases and in figures 8 and 9 for R1 flow cases. As for the R40 flow cases, the cross-stream and longitudinal planes at $Re_b = 1000$, shown in figures 6(a) and 7(a), highlight the onset of two symmetric large-scale ejections carrying low-speed fluid from the outer wall towards the channel core. These secondary motions are generated by two pairs of counter-rotating roll cells, which resemble closely Dean vortices. The inner-wall flow region is almost unaffected by these vortices, as one can see from figure 7(b). Figures 6(b) and 7(c), depicting the cross-stream and longitudinal planes at $Re_b = 4000$, show that fine-scale ejections and organised structures of momentum streaks characterise the outer wall, from which one can infer that the flow is fully turbulent. Traces of the streamwise vortices appear as streamwise-aligned bands of high-speed fluid near the inner wall, as visible in figure 7(d). Being centrifugally stable, the inner-wall flow region is still transitional, as no clear signs of turbulent activity appear. The cross-stream planes at $Re_b = 20\,000$ and $87\,000$ (figure 6c,d) show clear signs of streaky patterns at both walls. Overlaying the small scales of turbulence, streamwise large-scale structures are found near the outer wall, whose footprint appears in the wall-parallel planes of figures 7(e) and 7(g) as wide regions of alternating high and low speed fluid. These large-scale regions fill the entire streamwise extent of the domain, and their spanwise width is comparable to the channel height, hence two pairs of roll cells are present. The influence of the latter is found to extend to the inner wall at high Reynolds numbers. In fact, low-speed regions at the outer wall, corresponding to large-scale ejections, are found at the same spanwise location as high-speed regions at the inner wall, corresponding to large-scale sweeps (figure 7f,h).

Cross-stream visualisations show clearly how the region with higher momentum shifts towards the inner wall for the R1 flow cases (figure 8), as expected from the mean velocity profiles (figure 4). As well as for the R40 flow cases, signatures of streamwise roll cells are visible as large-scale ejections from the outer wall, although they are now more numerous and chaotic. As displayed in the wall-parallel plane of figure 9(a), streaky

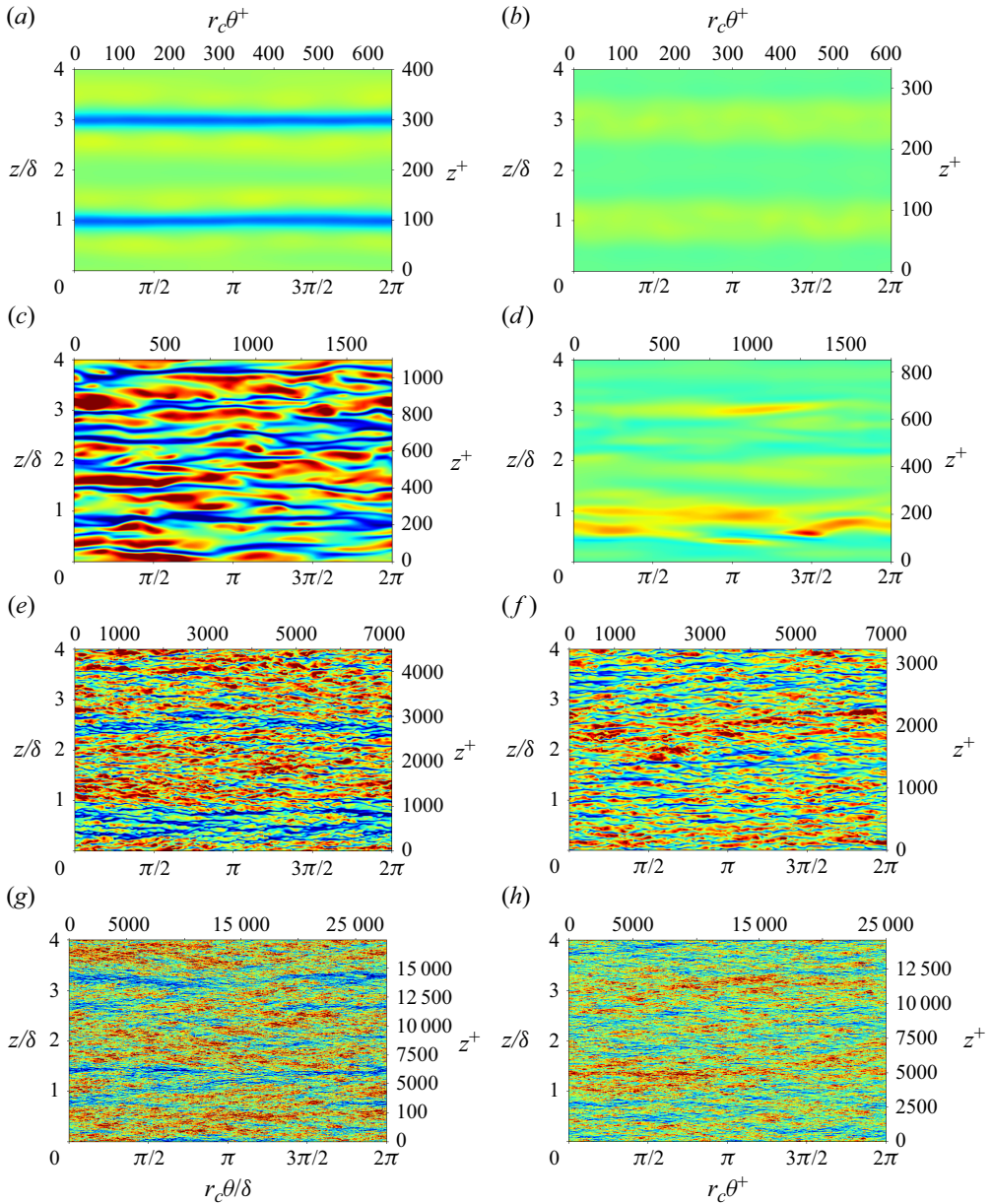


Figure 7. Instantaneous fields of streamwise velocity fluctuations for the R40 flow cases in wall-parallel planes near the outer (a,c,e,g) and inner wall (b,d,f,h) at $y^+ \approx 12$. The panels correspond to $Re_b = 1000$ (a,b), 4000 (c,d), 20 000 (e,f), 87 000 (g,h). The flooded contours range from $-0.3 u_b$ (blue) to $0.3 u_b$ (red). Streamwise and spanwise coordinates are shown in both outer units ($r_c \theta / \delta$, z / δ), and local wall units ($r_c \theta^+$, z^+), where the streamwise domain extent is measured at the centreline. Mean flow goes from left to right.

structures appear to be quite distinct at the outer wall at $Re_b = 1000$, confirming that increasing curvature promotes the transition to turbulence. Figure 9(c,e,g) show that momentum streaks at the outer wall exhibit a wavy pattern with a streamwise wavelength comparable to the domain size. This pattern resembles the ‘undulating Dean vortex flow’ found by Finlay *et al.* (1988), which is likely associated with inflectional instabilities of the

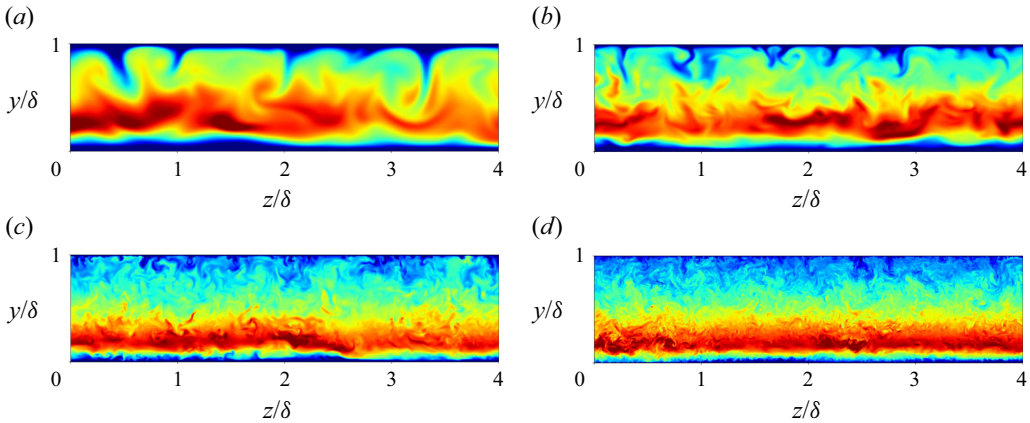


Figure 8. Instantaneous streamwise velocity fields in a cross-stream plane for the R1 flow cases at $Re_b = 1000$ (a), 4000 (b), 20 000 (c), 87 000 (d). The flooded contours range from $0.4 u_b$ (blue) to $1.5 u_b$ (red). Only half of the domain is shown.

wall-normal velocity profile (Le Cunff & Bottaro 1993), as evidenced by figures 4(b) and 5(b). The streaks are wider for the R1 flow cases than for R40, whereas streamwise large-scale structures are narrower, making the distinction between fine-scale turbulence and large-scale structures less clear cut. In fact, streamwise roll cells do not clearly show up in the wall-parallel planes of fluctuating streamwise velocity. This, however, does not convey that they are absent: as we shall see, in case of strong curvature these secondary motions are organised differently and mainly impact the wall-normal velocity. As visible from the wall-parallel planes shown in figure 9(b,d,f), the inner-wall flow region is devoid of turbulent structures, or nearly so for the highest Reynolds number (figure 9h), whereas it is characterised by the presence of large-scale structures elongated in the spanwise direction. The latter are visible in the form of alternating regions of high and low speed fluid aligned along the spanwise with length comparable to δ . The streamwise extent of each pair of spanwise structures is approximately $\pi\delta$, meaning that the computational domain can fit two pairs, with exception of the case $Re_b = 4000$, at which the streamwise wavelength seems slightly shorter.

3.3. Velocity spectra

A clearer understanding of the energetic relevance of the various scales of motions can be achieved from inspecting the spectra of the velocity fluctuations. Spectra of both streamwise and wall-normal velocity fluctuations are presented, the former to detect large-scale structures typical of plane channel flows (Lee & Moser 2015), whereas the latter are instrumental in revealing the presence of streamwise roll cells (Dai, Huang & Xu 2016). Figures 10 and 11 display the premultiplied spectra of streamwise velocity fluctuations in the spanwise ($k_z^* E_{uu}^*$) and streamwise ($k_\theta^* E_{uu}^*$) directions as a function of the distance from the wall for R40 and R1 flow cases, respectively. For clarity, we refer to the distance from the inner wall as $y_i = y$, and from the outer wall as $y_o = \delta - y$, both displayed on the left-hand vertical axis. The distance from the inner and outer wall is also reported on the right-hand vertical axis in local wall units, y_i^+ and y_o^+ , respectively.

In the R40 flow cases a primary energy peak appears in the spanwise spectra (figures 10a–c and 11a–c) near both walls at $y_i^+ \approx y_o^+ \approx 12$, $\lambda_z^+ \approx 100$, which is the typical signature of the regeneration cycle of momentum streaks (Hamilton, Kim & Waleffe

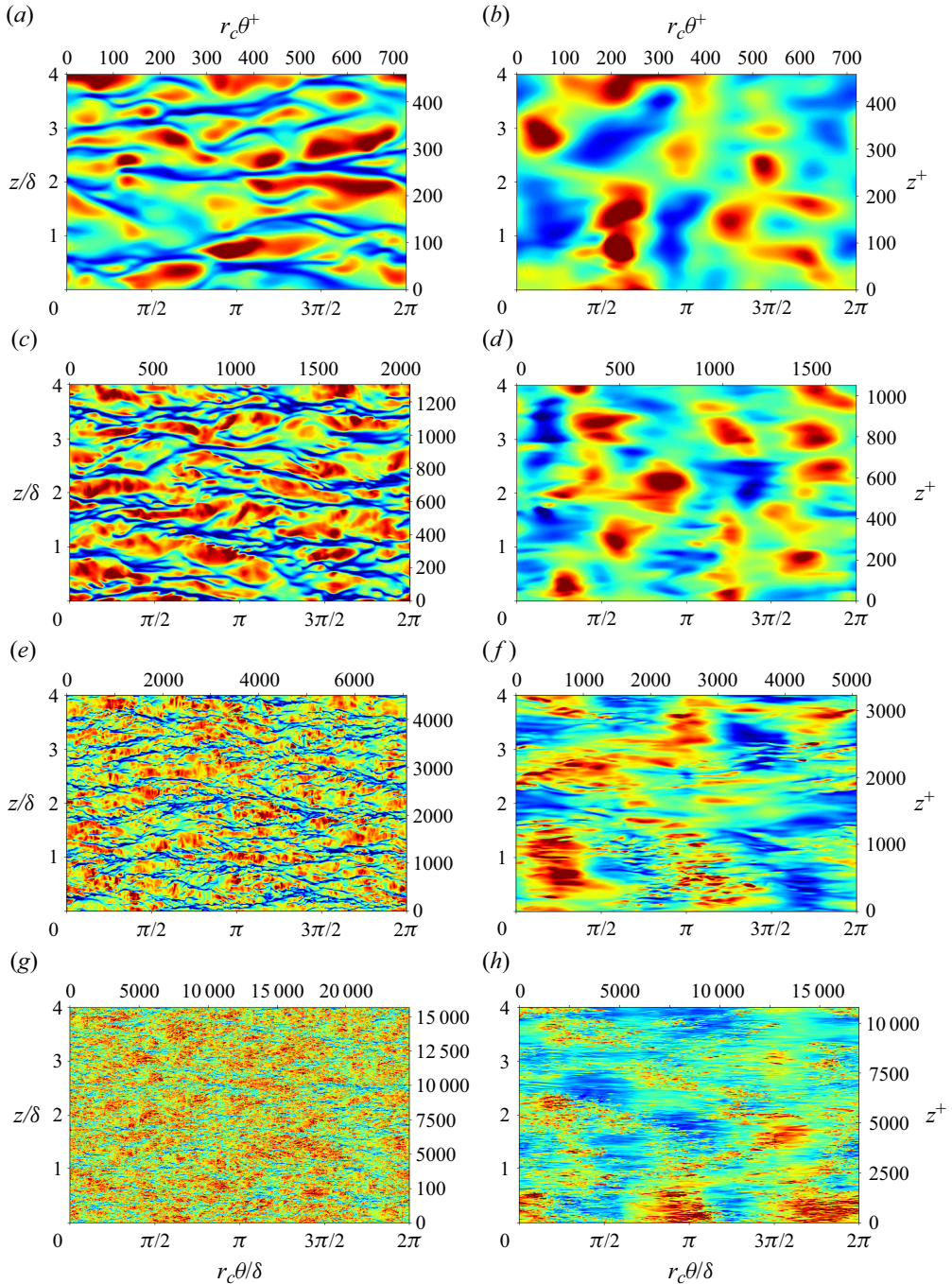


Figure 9. Instantaneous fields of streamwise velocity fluctuations for the R1 flow cases in wall-parallel planes near the outer (a,c,e,g) and inner wall (b,d,f,h) at $y^+ \approx 12$. The panels correspond to $Re_b = 1000$ (a,b), 4000 (c,d), 20 000 (e,f), 87 000 (g,h). The flooded contours range from $-0.3 u_b$ (blue) to $0.3 u_b$ (red). Streamwise and spanwise coordinates are shown in both outer units ($r_c\theta/\delta$, z/δ), and local wall units ($r_c^+\theta$, z^+), where the streamwise domain extent is measured at the centreline. Only half of the domain is shown.

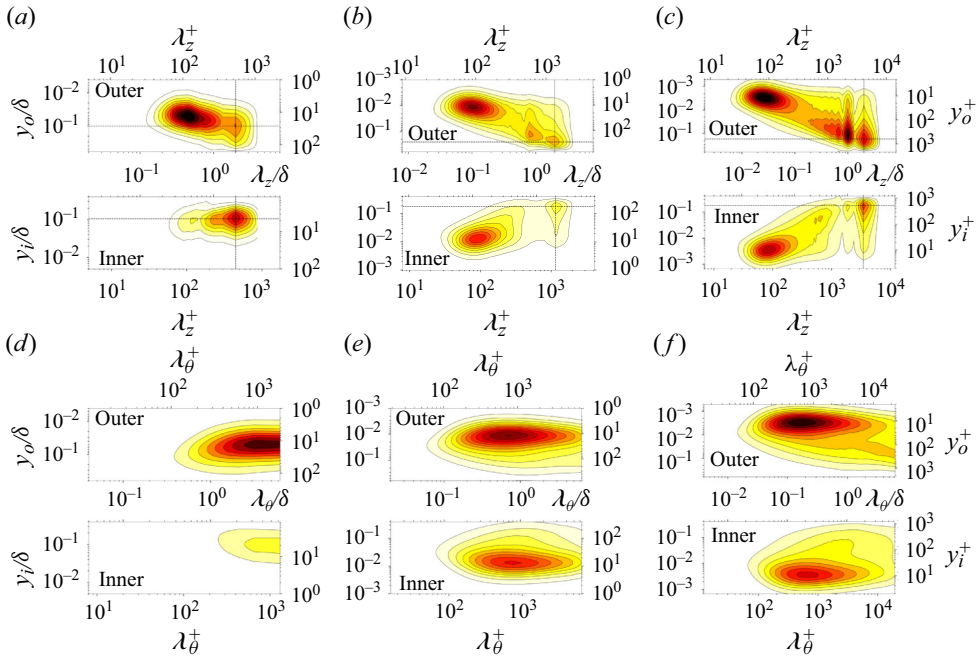


Figure 10. Premultiplied spectra of streamwise fluctuating velocity as a function of spanwise wavelength, $k_z^* E_{uu}^*$, (a–c) and of streamwise wavelength, $k_\theta^* E_{uu}^*$, (d–f) as the wall distance varies for the R40 flow cases. The panels correspond to $Re_b = 4000$ (a,d), 20 000 (b,e), 87 000 (c,f). Wall distance from the inner and outer wall, spanwise and streamwise wavelengths are reported in outer units (y_i/δ , y_o/δ , λ_z/δ , λ_θ/δ), and in local wall units (y_i^+ , y_o^+ , λ_z^+ , λ_θ^+), respectively. Dashed lines mark wavelength and wall distance of the energy peak associated with streamwise large-scale structures.

1995). An exception is the case at $Re_b = 4000$: the inner-wall primary peak is nearly absent, confirming the inferences from flow visualisations. From the streamwise spectra (figures 10d–f and 11d–f) we note that the streaks-related peak is at $\lambda_\theta^+ \approx 800$, meaning that the mean wavelength of momentum streaks is slightly shorter than the typical value of plane channel flows, namely $\lambda_x^+ \approx 1000$ (Monty *et al.* 2009). A secondary peak appears in the spanwise spectra farther from walls, at $y_i \approx y_o \approx 0.1\delta$ at $Re_b = 4000$ (figures 10a and 11a), and $y_i \approx y_o \approx 0.2\delta$ at $Re_b = 20\,000$ (figures 10b and 11b) and 87 000 (figures 10c and 11c). As seen from the intersection of the dashed lines, the energy of the peaks is concentrated at $\lambda_z/\delta \approx 2$. If the domain contains n pairs of roll cells, we expect to find a peak in the spanwise spectra at $\lambda_z = L_z/n$, where $L_z = 4\delta$ for the R40 flow cases. Flow visualisations indeed revealed the presence $n = 2$ roll cells pairs, hence we interpret these peaks as the footprint of streamwise large-scale structures. A third peak at $\lambda_z/\delta \approx 1$ appears faintly at $Re_b = 20\,000$, and sharply emerges at $Re_b = 87\,000$. This peak corresponds to $n = 4$ pairs of streamwise cells, indicating that roll cells with various sizes could be present, which we will investigate below. The streamwise spectra reveal that the scales of motion with the maximum streamwise wavelength, $\lambda_\theta = L_\theta = 2\pi$, are quite energetic, suggesting that the streamwise vortices span the whole domain along the streamwise direction.

As for the R1 flow cases (figure 11) the primary peak in the spanwise spectra due to momentum streaks appears on the outer wall only, suggesting that the near-wall turbulence regeneration cycle still takes place at the outer wall (figure 11a–c). As noted in flow visualisations, streaky structures have a greater spanwise wavelength than the R40 flow

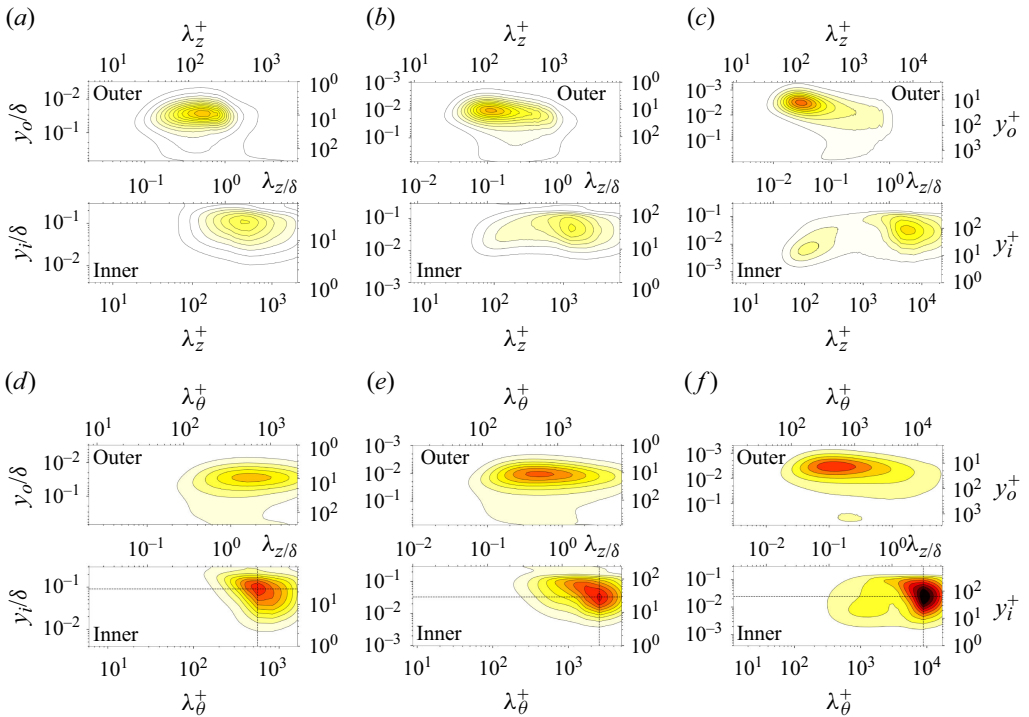


Figure 11. Premultiplied spectra of streamwise fluctuating velocity as a function of spanwise wavelength $k_z^* E_{uu}^*$, (a–c) and of streamwise wavelength, $k_\theta^* E_{uu}^*$, (d–f) as the wall distance varies for the R1 flow cases. The panels correspond to $Re_b = 4000$ (a,d), 20 000 (b,e), 87 000 (c,f). Wall distance from the inner and outer wall, spanwise and streamwise wavelengths are reported in outer units (y_i/δ , y_o/δ , λ_z/δ , λ_θ/δ), and in local wall units (y_i^+ , y_o^+ , λ_z^+ , λ_θ^+), respectively. Dashed lines mark wavelength and wall distance of the energy peak associated with spanwise large-scale structures.

cases, which is approximately $\lambda_z^+ \approx 120$. Their streamwise wavelength is instead shorter, approximately $\lambda_\theta^+ \approx 500$, as visible from the streamwise spectra (figure 11d–f). The absence of a primary peak near the inner wall in the spanwise spectra highlights the stabilising effect of convex curvature. More specifically, the near-wall peak is absent at $Re_b = 4000$ (figure 11d), starts to form at $Re_b = 20\,000$ (figure 11e), and only becomes visible at $Re_b = 87\,000$ (figure 11f). This trend, which is also found in the streamwise spectra, suggests that the inhibiting effect of convex curvature on turbulence becomes gradually less intense as the Reynolds number increases. In contrast to the R40 flow cases, never does a secondary peak emerge in the spanwise spectra near the outer wall. This implies that the streamwise roll cells, if present, have a negligible effect on the streamwise velocity fluctuations. A secondary peak is instead present near the inner wall at $\lambda_z/\delta \approx 2$, which moves closer to the wall (in δ units) as Re_b increases. This peak cannot be related to streamwise roll cells for two reasons: (i) they are most intense at the outer wall, yet no secondary peak is detected there, and (ii) the spanwise wavelength of streamwise vortices must be shorter, as one can infer from figure 8 and as we will show more clearly below. Rather, we can ascribe this peak to the presence of spanwise large-scale structures. To substantiate this statement, we consider the streamwise energy spectra, which highlight energetic modes near the inner wall at long wavelengths: $\lambda_\theta/\delta \approx 2\pi/3$ at $Re_b = 4000$ (figure 11d) and $\lambda_\theta/\delta \approx \pi$ at 20 000 (figure 11e) and 87 000 (figure 11f), as marked by the dashed lines. These energy peaks cannot be related either to turbulence structures,

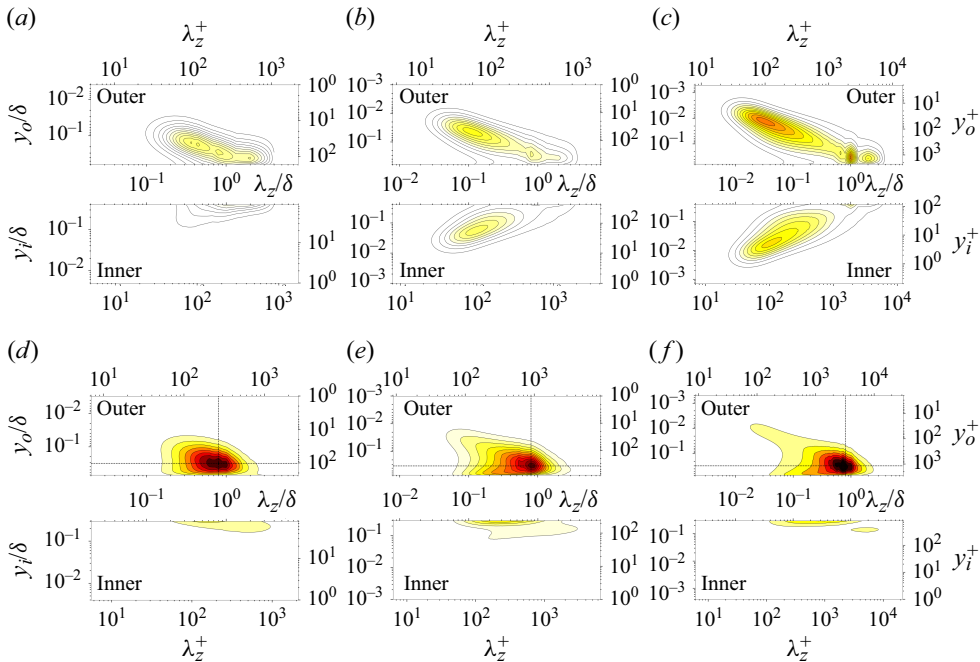


Figure 12. Premultiplied spectra of fluctuating wall-normal velocity ($k_z^* E_{vv}^*$) as a function of the spanwise wavelength and wall distance for the R40 flow cases (a–c) and R1 flow cases (d–f). The panels correspond to $Re_b = 4000$ (a,d), 20 000 (b,e), 87 000 (c,f). Wall distance from the inner and outer wall and spanwise wavelength are reported in outer units (y_i/δ , y_o/δ , λ_z/δ) and local wall units (y_i^+ , y_o^+ , λ_z^+), respectively. Dashed lines mark the wavelength and wall-distance of the energy peak related to streamwise large-scale structures.

which are absent or strongly inhibited near the inner wall, or to streamwise roll cells, as we have just seen through the spanwise spectra that they do not affect streamwise velocity fluctuations. However, flow visualisations in wall-parallel planes near the inner wall (figure 9b,d,f) revealed the presence of spanwise structures, organised in pairs with a streamwise length of approximately $\pi\delta$. The wavelength of these peaks corresponds to $n = L_\theta/\lambda_\theta = 3$ pairs of eddies at $Re_b = 4000$ and $n = L_\theta/\lambda_\theta = 2$ pairs at 20 000 and 87 000. Hence, we interpret the energy peaks in the streamwise spectra as the signature of cross-flow structures. Moreover, the spanwise size of these structures is comparable to δ , explaining the peaks in the spanwise spectra at $\lambda_z/\delta \approx 2$.

In figure 12 we show the premultiplied spectral densities of wall-normal velocity fluctuations in the spanwise direction ($k_z^* E_{vv}^*$). In the R40 flow cases (figure 12a–c) energy peaks related to near-wall turbulent structures form at $y_i^+ \approx y_o^+ \approx 50$, $\lambda_z^+ \approx 100$, except for the inner wall at $Re_b = 4000$, in agreement with the flow visualisations. Two secondary peaks in the channel core, more prominent at $Re_b = 87\,000$, highlight the presence of energetic modes with $\lambda_z/\delta \approx 1$ and $\lambda_z/\delta \approx 2$ at $y_o/\delta \approx 0.3$. Following the same reasoning about the streamwise velocity spectra, we trace these energetic modes to streamwise roll cells, which generate large-scale radial sweeps and ejections.

The effect of strong curvature on the energy distribution of the wall-normal velocity fluctuations (figure 12d–f) is rather striking. Contrary to the streamwise velocity spectra, the energy content is now much higher in the case of strong curvature, which points to substantial structural changes. No distinct peak is observed in the inner part of the channel, which conveys that the spanwise large-scale structures that we noted above have no impact

(on average) on the wall-normal velocity fluctuations. A prominent energy peak is located at $y_o \approx 0.3\delta$, $\lambda_z \approx 0.8\delta$, marked by the intersection of the dashed lines. This energetic mode is not present in plane channel flow (see e.g. Cho, Hwang & Choi 2018) and cannot be related to cross-flow structures, which are more intense near the inner wall. Hence, we interpret them as the signatures of streamwise roll cells. This would mean that the typical configuration of streamwise large-scale structures consists of $n = L_z/\lambda_z = 10$ pairs of roll cells (with $L_z = 8$, $\lambda_z = 0.8\delta$), which we will ascertain in the following.

3.4. Streamwise large-scale structures

Flow visualisations and energy spectra reveal the presence of streamwise large-scale structures, which are akin to the Dean vortices observed in laminar flow (Dean 1928). To understand how these structures depend on curvature and Reynolds number and how they affect the flow field, we separate the coherent contribution from the underlying turbulence, where coherence is intended in the sense given by Hussain (1986). For that purpose we use the triple decomposition of Hussain & Reynolds (1970), whereby a generic field variable, $\varphi(\theta, r, z, t)$, is decomposed as

$$\varphi(\theta, r, z, t) = \Phi(r) + \tilde{\varphi}(r, z, t) + \varphi''(\theta, r, z, t), \quad (3.6)$$

where Φ is the space average over the homogeneous directions (θ, z) and time (t),

$$\tilde{\varphi}(r, z, t) = \langle \varphi(\theta, r, z, t) \rangle_\theta - \Phi(r), \quad (3.7)$$

is the coherent contribution from the streamwise vortices, $\langle \varphi(\theta, r, z, t) \rangle_\theta$ is the average over the streamwise direction, and

$$\varphi''(\theta, r, z, t) = \varphi(\theta, r, z, t) - \langle \varphi(\theta, r, z, t) \rangle_\theta \quad (3.8)$$

is the instantaneous turbulent fluctuation. The total fluctuation is then $\varphi' = \tilde{\varphi} + \varphi''$. The instantaneous streamwise-averaged fields ($\tilde{\varphi}$) are then averaged over time to extract the coherent contribution, namely $\overline{\tilde{\varphi}}$. One should note that, in principle, the averages defined in (3.7) would be zero in infinitely long domains, and their long-time averages would also tend to zero. Hence, the coherent motions herein considered refer to a finite streamwise length associated with the extent of the computational domain (here, $L_\theta = 2\pi\delta$), and to a finite time horizon, here taken to be $600\delta/u_b$. Whereas the intensity of those coherent motions is inevitably affected by these choices (see appendix D), the conclusions regarding the influence of Reynolds number and wall curvature still stand.

In figure 13 we show the Stokes stream function for streamwise-coherent motions ($\overline{\tilde{\psi}}$), defined such that $\tilde{w} = \partial\tilde{\psi}/\partial r$, $\tilde{v} = -\partial\tilde{\psi}/\partial z$. The overlaid flooded contours represent the mean coherent streamwise velocity ($\overline{\tilde{u}}$). In addition, we report the spanwise distribution of the mean shear at the inner and outer wall,

$$\overline{\tau}_{w,i}^+(z) = \frac{\nu}{u_{\tau,i}^2} \frac{\partial \overline{\langle u \rangle}_\theta}{\partial r} \Big|_{r_i}, \quad \overline{\tau}_{w,o}^+(z) = \frac{\nu}{u_{\tau,o}^2} \frac{\partial \overline{\langle u \rangle}_\theta}{\partial r} \Big|_{r_o}. \quad (3.9)$$

In the R40 flow cases (figure 13a–c) two pairs of counter-rotating vortices appear which nearly span the whole channel thickness and with a spanwise wavelength $\lambda_z/\delta \approx 2$, which is in agreement with the energy spectra in figure 10. Streamwise roll cells with the same size were detected by Moser & Moin (1987). The spanwise inhomogeneity due to these secondary eddies has a strong impact on the distribution of the wall shear stress. Indeed, large-scale ejections are generated between any pair of counter-rotating vortices (blue contours), where low-speed fluid is diverted away from the wall, and local friction attains a minimum. Correspondingly, large-scale sweeps generate at the opposite wall whereby

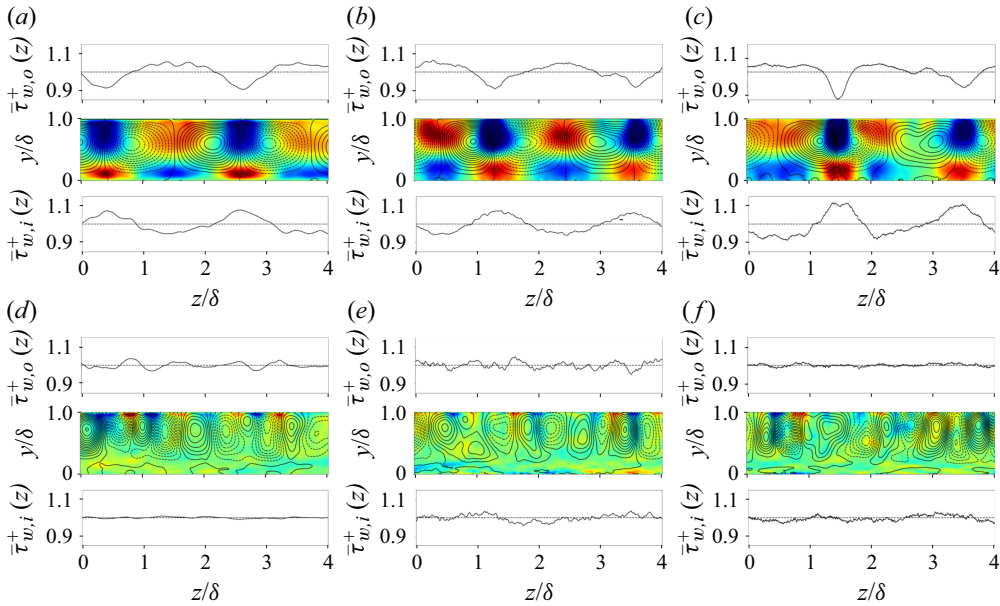


Figure 13. Mean Stokes stream function ($\bar{\psi}$) for streamwise-coherent disturbances in an (r, z) -plane overlaid to flooded contours of coherent streamwise velocity (\bar{u}), for the R40 flow cases (a–c) and for the R1 flow cases (d–f). The panels correspond to $Re_b = 4000$ (a,d), 20 000 (b,e), 87 000 (c,f). Positive values of $\bar{\psi}$ (solid lines) indicate a clockwise-rotating roll cell, and *vice versa* for negative values (dashed lines). The flooded contours range from $-1.5 u_{\tau,g}$ (blue) to $1.5 u_{\tau,g}$ (red). Each panel shows the spanwise distribution of the mean shear stress at the two walls, $\bar{\tau}_{w,i}^+(z)$ and $\bar{\tau}_{w,o}^+(z)$, defined in (3.9). Only half of the domain is shown for the R1 flow cases.

high-speed fluids is pushed towards the wall (red contours), causing local increase of wall friction. This tendency is clearer as the Reynolds number increases, as one can infer from the spanwise distribution of the local wall shear, which shows excursions of approximately 10 % at $Re_b = 4000$ (figure 13a) and $Re_b = 20\,000$ (figure 13b), and reaching up to 20 % at $Re_b = 87\,000$ (figure 13c).

As for the R1 flow cases (figure 13d–f), the number of pairs of counter-rotating vortices increases to approximately 10 (only five are visible as half of the domain is shown). Hence, the spanwise wavelength of the roll cells is $\lambda_z/\delta \approx 0.8$, which again corresponds to what found from the spectral analysis in figure 12. Spanwise shortening of the streamwise roll cells is also observed in rotating channel flows, in which similar vortices develop on account of Coriolis forces (Matsson & Alfredsson 1990). Through DNS of rotating channel flow, Brethouwer (2017) found that the size of the streamwise roll cells is smaller at higher rotation numbers (the rotation number in rotating channel flow is the counterpart of the curvature ratio in curved channels), in agreement with previous numerical studies (Kristoffersen & Andersson 1993; Yang & Wu 2012). In addition, Brethouwer (2017) found that the size of the roll cells is independent of the Reynolds number, which is also the case here. Due to strong channel curvature, the roll cells are pushed towards the outer wall and cannot fill the entire channel thickness. Hence, the flow region near the inner wall (say, $y/\delta < 0.2$) is not affected, as seen in the spanwise distribution of the wall shear, which is nearly flat. As for the shear at the outer wall, spanwise excursions of $\bar{\tau}_{w,o}^+(z)$ have a maximum amplitude of approximately 4 % at $Re_b = 4000$ (figure 13d) and $Re_b = 20\,000$ (figure 13e), whereas they are very small at $Re_b = 87\,000$ (figure 13f), at which the effect

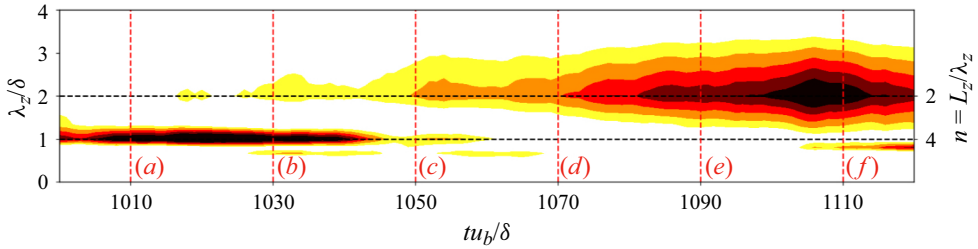


Figure 14. Time history of the premultiplied spanwise energy spectra of fluctuating streamwise velocity ($\lambda_z^* E_{uu}^*$) for the R40 flow case at $Re_b = 87\,000$, at $y/\delta = 0.8$. The black dashed lines correspond to $\lambda_z/\delta = 2$ and $\lambda_z/\delta = 1$, at which the expected number of streamwise vortices are indicated on the right vertical axis.

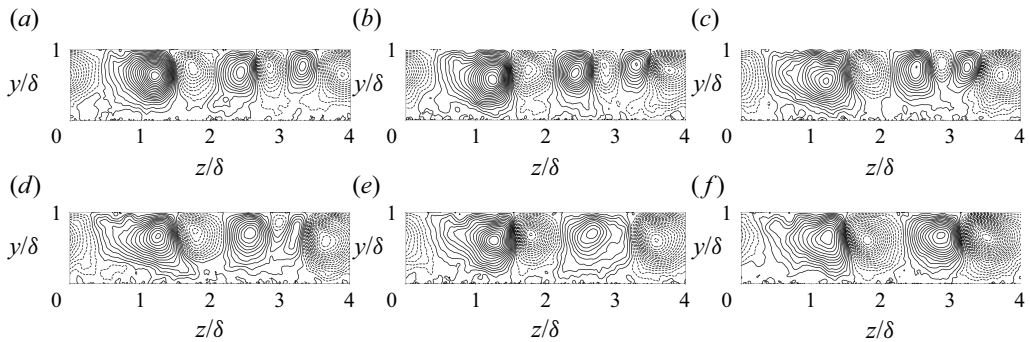


Figure 15. Coherent stream function ($\tilde{\psi}$) at the time instants marked by the red dashed lines in [figure 14](#), for the R40 flow case at $Re_b = 87\,000$.

of the streamwise vortices is outweighed by turbulence. The reason why the outer-wall shear stress is barely affected by streamwise vortices is their unsteadiness. The coherent stream function shows indeed that roll cells are less organised in the R1 flow cases than in R40, and on average they do not affect the streamwise velocity. Nonetheless, the impact of those eddies on the instantaneous flow is certainly not negligible in the case of strong curvature. The strength of streamwise large-scale structures can be quantified in terms of the maximum amplitude of the coherent wall-normal velocity (Canton *et al.* 2016), which results in $\max|\tilde{v}|/u_b \approx 6\%$ for the R40 flow cases, nearly independent of the Reynolds number. Streamwise vortices in the R1 flow cases are much stronger, their strength being $\max|\tilde{v}|/u_b \approx 20\%$ at $Re_b = 4000$ and 12% at $87\,000$.

3.5. Splitting and merging events

The eduction procedure based on triple decomposition allowed to quantify the statistical organisation of streamwise large-scale structures. However, the energy spectra highlighted the presence of multiple peaks at large wavelengths, which are particularly evident for the R40 flow case at $Re_b = 87\,000$ ([figure 10](#)). Multiple peaks suggest either the coexistence of large-scale structures of different sizes, or the occurrence of splitting and merging events. To clarify this point, we inspect the time history of the spanwise energy spectra of streamwise velocity fluctuations, shown in [figure 14](#) for the R40 flow case at $Re_b = 87\,000$, at the wall distance where the peak of the energy associated with the streamwise vortices occurs. A time window from $tu_b/\delta = 1000$ to 1120 was selected for the analysis and we took six subsequent snapshots of $\tilde{\psi}$, shown in [figure 15](#), at intervals of $20\delta/u_b$

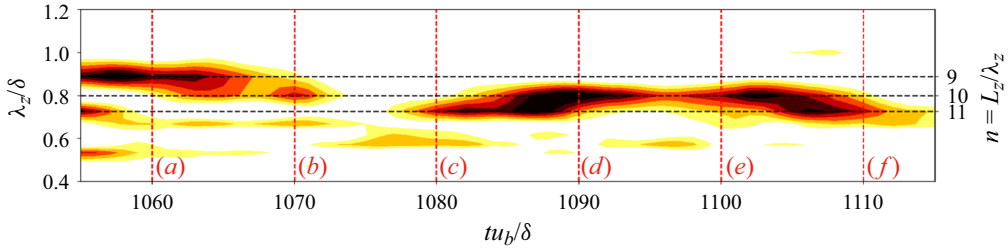


Figure 16. Time history of the premultiplied spanwise energy spectra of fluctuating wall-normal velocity ($k_z^* E_{vv}^*$) for the R1 flow case at $Re_b = 87\,000$, at $y/\delta = 0.7$. The black dashed lines correspond to $\lambda_z/\delta = 0.73$, $\lambda_z/\delta = 0.80$ and $\lambda_z/\delta = 0.89$, at which the expected number of streamwise vortices are indicated on the right-hand vertical axis.

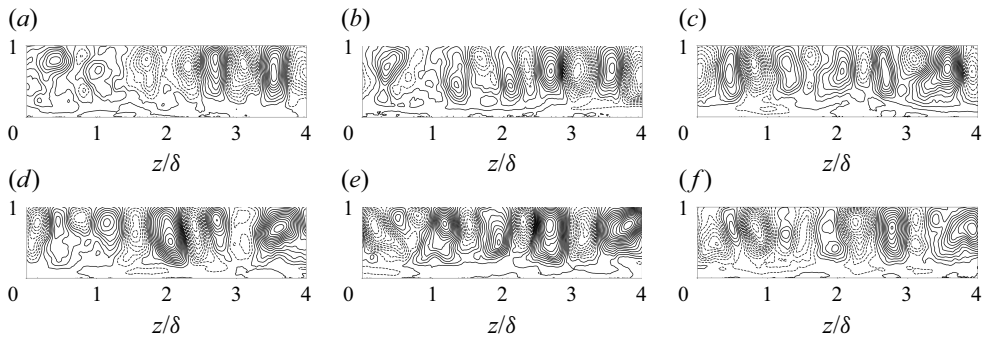


Figure 17. Coherent stream function ($\tilde{\psi}$) at the time instants marked by the red dashed lines in figure 16 for the R1 flow case at $Re_b = 87\,000$. Only half of the domain is shown.

marked by the red dashed lines in figure 14. From $tu_b/\delta \approx 1000$ to 1040 most energy is clustered around $\lambda_z/\delta = 1$, hence $n = 4$ pairs of vortices would be expected (the number of vortices pairs is indicated on the right-hand vertical axis). However, the snapshots of $\tilde{\psi}$ at $tu_b/\delta \approx 1010$ (figure 15a) and 1030 (figure 15b) reveal the occurrence of $n = 3$ pairs. In this respect, we note that the roll cells are not uniform in size, as the pair centred at $z/\delta \approx 0.5$ has a wavelength $\lambda_z/\delta \approx 2$, whereas the two remaining pairs have a wavelength $\lambda_z/\delta \approx 1$. A possible explanation is that the two pairs of small-size vortices are stronger than the large-size one, hence more energy is concentrated at $\lambda_z/\delta = 1$. A vortex-merging event is observed between $tu_b/\delta \approx 1050$ and 1090. Figures 15(c) and 15(d) depict that the pair of smallest vortices located at $z/\delta \approx 3$ decrease in size and strength, as the isolines of the stream function get sparser. This process continues until the smallest pair is embedded within the adjacent clockwise rotating vortex (figure 15e), which appears more regular and strong at $tu_b/\delta \approx 1110$ (figure 15f). From $tu_b/\delta \approx 1080$ on, the energy peak is clustered around $\lambda_z/\delta = 2$ and, as expected, $n = 2$ pairs of roll cells are found.

The results obtained for the R1 flow case at $Re_b = 87\,000$ are presented in figure 16, which reports the time evolution of the spanwise spectra of the wall-normal velocity at the peak position of energy associated with the streamwise vortices. The time window under scrutiny is half as for the R40 flow case, and the six subsequent snapshots of $\tilde{\psi}$, shown in figure 17, are sampled at intervals of $10\delta/u_b$ instead of 20 on account of stronger unsteadiness in cases with strong curvature. The time evolution of the spectra shows that

the energy peak is clustered around $\lambda_z/\delta \approx 0.89$ from $tu_b/\delta = 1055$ to 1065. Consistently, [figure 17\(a\)](#) displays nine vortices in the region under scrutiny ($n = 9$ pairs are present in the whole domain). This configuration seems to be unstable because of the lack of organisation of the vortex pair located at $z/\delta \approx 1$, and because two anticlockwise vortices are adjacent straddling $z/\delta \approx 2$. At $tu_b/\delta = 1070$ the energy peak shifts at $\lambda_z/\delta \approx 0.8$, indeed the related [figure 17\(b\)](#) shows that a new clockwise rotating vortex emerged at $z/\delta \approx 2.2$ fitting in between the two anticlockwise rotating vortices and increasing the number of vortices to 10 (i.e. $n = 10$). The number of vortex pairs increase further to $n = 11$ at $tu_b/\delta \approx 1080$, as visible in [figure 17\(c\)](#), and the energy peak decreases accordingly to $\lambda_z/\delta \approx 0.73$. From $tu_b/\delta \approx 1085$ to 1105 the energy peak settles at $\lambda_z/\delta \approx 0.8$, and [figures 17\(d\)](#) and [17\(e\)](#) highlight that the vortex configuration consists of $n = 10$ pairs. The energy peak shifts again to $\lambda_z/\delta \approx 0.73$ at $tu_b/\delta = 1110$. [Figure 17\(f\)](#) shows that the main vortices are still 10, however, small secondary vortices tend to split off from the primary ones, bringing more energy to smaller scales. In the case of strong curvature, the transitions from one vortex configuration to the other can be attributed to the unsteady dynamics of the vortices, which can be inferred from their spanwise motions, distorted shapes and different sizes, rather than to splitting and merging phenomena, which could not be clearly identified.

3.6. Role of streamwise vortices on velocity fluctuations

In [figure 18](#) we show the root-mean-square (r.m.s.) of the streamwise ([figure 18a,b](#)) and wall-normal ([figure 18c,d](#)) velocity fluctuations, as well as the turbulent shear stress ([figure 18e,f](#)). Total fluctuations are reported along with the contributions due to the streamwise vortices, which we have determined by taking the r.m.s. of the coherent contribution (3.7) along the spanwise direction and in time. For the R40 flow cases, the streamwise velocity fluctuations ([figure 18a](#)) are higher at the outer than at the inner wall. As made clear from the increased intensity of the coherent fluctuations, this asymmetry is mainly due to the streamwise vortices, which are stronger near the outer wall. An exception is the case at $Re_b = 4000$ (green line), in which the coherent contribution at the outer wall is comparable to that at the inner wall. In general, the coherent contribution is approximately half of the total. The peak of the coherent contribution occurs between $y/\delta \approx 0.8$ and $y/\delta \approx 0.9$, corresponding to a bump in the profile of the total fluctuations. As for the R1 flow cases, the profiles of streamwise velocity fluctuations ([figure 18b](#)) show a near-wall peak on the concave side comparable to that of the corresponding R40 flow cases, and little contribution from coherent fluctuations. The profile of the velocity fluctuations is almost flat in the channel core, and the near-wall peak on the convex side is very different from the case with mild curvature, extending much farther from the wall. Wall-normal velocity fluctuations ([figure 18c](#)) are only relevant in the channel core, with a peak at $y/\delta \approx 0.7$. For the R1 flow cases ([figure 18d](#)) fluctuations of wall-normal velocity are up to two times larger than the streamwise velocity. Substantial contribution is found to be provided by the coherent fluctuations, which also attain a peak at $y/\delta \approx 0.7$, as observed in the velocity spectra.

As for the turbulent shear stress, it is nearly symmetrical in fully turbulent R40 flow cases ([figure 18e](#)), resembling the case of a plane channel (see e.g. Kim *et al.* 1987). However, two differences should be noted: (i) the point of zero crossing is shifted towards the inner wall at $y/\delta \approx 0.4$, and (ii) the peak value increases near the outer wall and decreases near the inner wall. The effect of convex curvature is particularly evident at $Re_b = 4000$, at which the zero crossing is even closer to the inner wall. The coherent turbulent stress is approximately half of the total at $y/\delta \approx 0.8$, pointing to significant

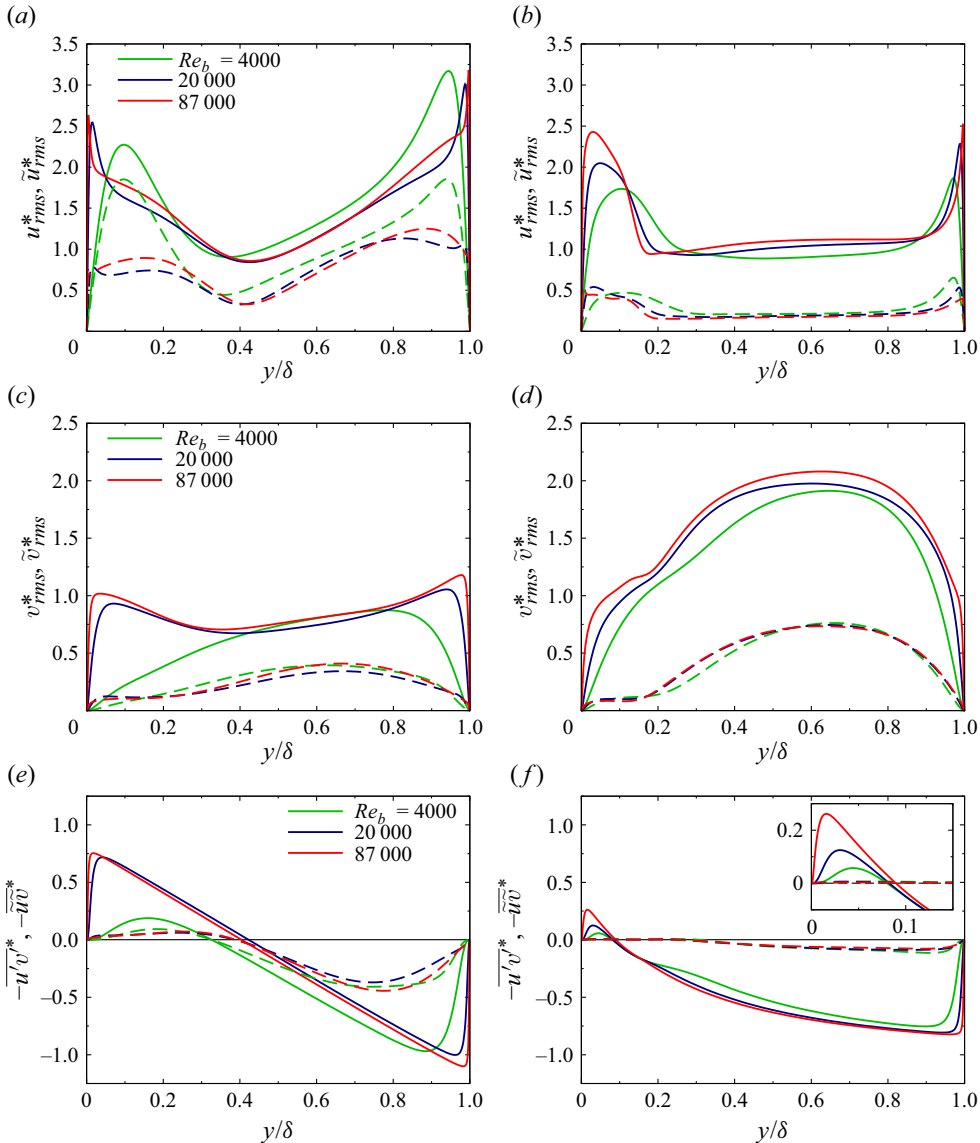


Figure 18. Profiles of r.m.s. streamwise (a,b) and wall-normal (c,d) velocity fluctuations and mean turbulent shear stress (e,f) at various Reynolds numbers for the R40 flow cases (a,c,e) and R1 flow cases (b,d,f). Solid lines refer to total fluctuations and dashed lines refer to coherent fluctuations due to streamwise vortices.

contribution of streamwise vortices to momentum transport. Similar conclusions were also reached by Moser & Moin (1987) and Brethouwer (2022). The effects of strong curvature are shown in figure 18(f). In the channel core, where viscous effects are negligible, the turbulent stress profile becomes quadratic rather than linear, as after the analytical distribution of the total shear stress (C2). As seen in the inset of figure 18(f), the peak value is greatly reduced near the inner wall, which aligns with the findings of So & Mellor (1973) in experiments of turbulent boundary layers over a convex surface. The reduction in turbulent shear stress at the inner wall is not only due to the stabilising effect of convex curvature but also results from the influence of spanwise large-scale

structures, as will be discussed below. The coherent Reynolds stress is negligible and vanishes entirely near the inner wall, as the streamwise vortices are displaced towards the outer wall (see § 3.4). This analysis demonstrates that strong curvature significantly alters the role of streamwise-aligned coherent structures in turbulence. Specifically, their contribution to wall-normal fluctuations becomes substantially larger than to streamwise fluctuations, while their contribution to momentum transport is suppressed.

3.7. Spanwise large-scale structures

Visualisations of the flow near the inner wall of strongly curved channels (figure 9) revealed the presence of alternating regions with positive/negative velocity fluctuations elongated along the spanwise direction. Those wavy patterns are the footprint of spanwise large-scale structures, which are originated from streamwise instabilities (Finlay *et al.* 1988) and which are convected at the mean flow speed (Matsson & Alfredsson 1992). As we did for the streamwise vortices, we exploit triple decomposition to separate the effects of the cross-stream structures from those of turbulence. A generic field variable, $\varphi(\theta, r, z, t)$, is decomposed as

$$\varphi(\theta, r, z, t) = \Phi(r) + \hat{\varphi}(\theta, r, t) + \varphi'''(\theta, r, z, t), \quad (3.10)$$

where

$$\hat{\varphi}(\theta - tu_c/r, r, t) = \langle \varphi(\theta, r, z, t) \rangle_z - \Phi(r), \quad (3.11)$$

is the spanwise-coherent contribution, $\langle \varphi(\theta, r, z, t) \rangle_z$ is the average along the spanwise direction, and $\varphi'''(\theta, r, z, t)$ is the instantaneous turbulent fluctuation. Since spanwise-aligned structures are advected with the flow, phase alignment is required to educe the associated coherent contribution. Hence, the time averages are evaluated by shifting consecutive spanwise-averaged field by an angle $\Delta t_s u_c / r_c$, where Δt_s is the sampling interval, set equal to a time unit, and u_c is the convection velocity of coherent disturbances. The convection velocity was estimated from the analysis of the wavenumber-frequency spectra of the streamwise velocity fluctuations for the R1 flow case at $Re_b = 4000$, resulting in $u_c \approx 0.67u_b$ (see appendix E), which is comparable to the value of $u_c \approx 0.80u_b$ found in experiments (Matsson & Alfredsson 1992). Moreover, the convection velocity in inner units is $u_c^+ \approx 11$, which is similar to the mean speed of the near-wall energy-containing eddies (Kim & Hussain 1993; Jimenez *et al.* 2001). This value of u_c was also considered for the flow cases at higher Reynolds number, as it was found to ensure maximum coherence in time.

In figure 19 we show the mean Stokes stream function for spanwise-coherent motions ($\hat{\psi}$), defined such that $\hat{v} = (\partial \hat{\psi} / \partial \theta) / r$, $\hat{u} = -\partial \hat{\psi} / \partial r$, overlaid to flooded contours of the mean coherent pressure (\hat{p}) in the (θ, r) -plane. Alternating high- and low-pressure regions are observed, marking the presence of spanwise large-scale structures. Those are organised into three pairs of roll cells at $Re_b = 4000$ (figure 19a), whereas only two pairs are found at $Re_b = 20\,000$ (figure 19b) and $87\,000$ (figure 19c). Although the radial extent of the spanwise structures is comparable to δ , they are most intense near the inner wall and weaker towards the outer wall. The stream function shows that the cross-stream structures have an irregular shape and tend to split up at high Reynolds number. This more chaotic organisation yields reduced strength of the spanwise structures, as measured in terms of the magnitude of the coherent streamwise velocity, $\max|\hat{u}|$. Indeed, we found $\max|\hat{u}|/u_b \approx 9\%$ at $Re_b = 4000$ and $\max|\hat{u}|/u_b \approx 7\%$ at $20\,000$ and $87\,000$, hence spanwise large-scale structures are approximately half as strong as the streamwise ones (see § 3.4). The centres of the roll cells are approximately at the same location as

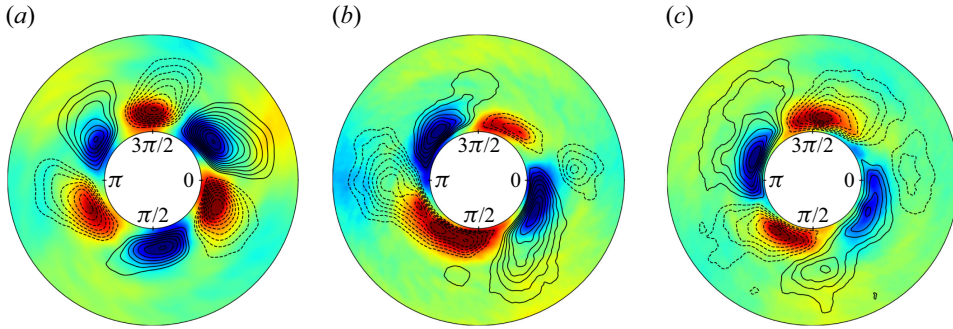


Figure 19. Mean Stokes stream function ($\overline{\psi}$) for spanwise-coherent disturbances, overlaid to flooded contours of the mean coherent pressure ($\overline{\hat{p}}$) in a (θ, r) -plane for the R1 flow cases at $Re_b = 4000$ (a), 20 000 (b), 87 000 (c). The flooded contours range from $-0.3u_{\tau,g}^2$ (blue) to $0.3u_{\tau,g}^2$ (red). Positive values of $\hat{\psi}$ (solid lines), indicate a clockwise-rotating roll cell, associated with negative coherent pressure (blue contours), whereas negative (dashed lines) correspond to anticlockwise rolls and positive coherent pressure (red contours). The mean flow is clockwise.

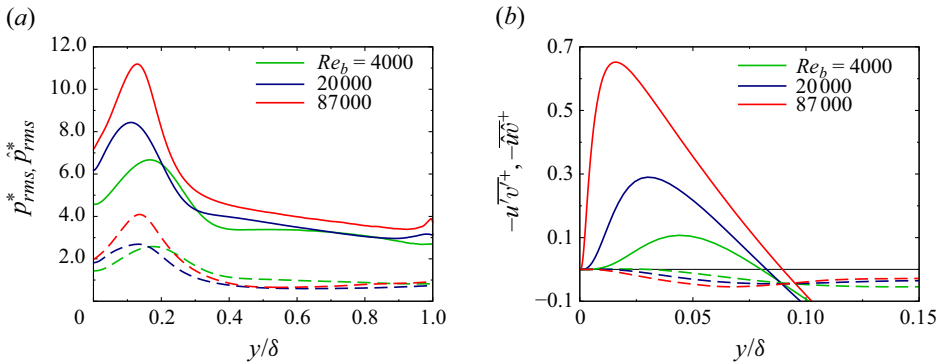


Figure 20. Profiles of r.m.s. pressure fluctuations (a) and mean turbulent stress near the inner wall (b) at various Reynolds numbers, for the R1 flow cases. Solid lines refer to total fluctuations and dashed lines refer to coherent fluctuations due to spanwise large-scale structures (the latter are denoted with the hat symbol).

the local minima of the mean shear rate (figure 5), supporting the idea that the spanwise structures may originate from a shear-layer instability (Finlay *et al.* 1988; Yu & Liu 1991).

Figure 20(a) displays the distributions of the r.m.s. pressure fluctuations for the R1 flow cases, and includes the contribution of coherent fluctuations due to the spanwise structures, which are obtained from the spanwise-coherent contribution according to (3.11). Near the inner wall, pressure fluctuations attain a peak which is twice as high as the outer wall at $Re_b = 4000$, and almost four times as high at $Re_b = 87\,000$. The impact of the spanwise-aligned structures on pressure fluctuations is substantial, as the peak value of the coherent contribution near the inner wall is approximately one third of the total. Another effect of spanwise structures, which is related to the increase of pressure fluctuations, is the suppression of the turbulent shear stress. This can be ascertained in figure 20(b), where we show the total turbulent stress (solid lines) and the coherent turbulent stress due to spanwise structures (dashed lines). The coherent turbulent shear stress yields a negative contribution, conveying that the spanwise structures tend to suppress ejections

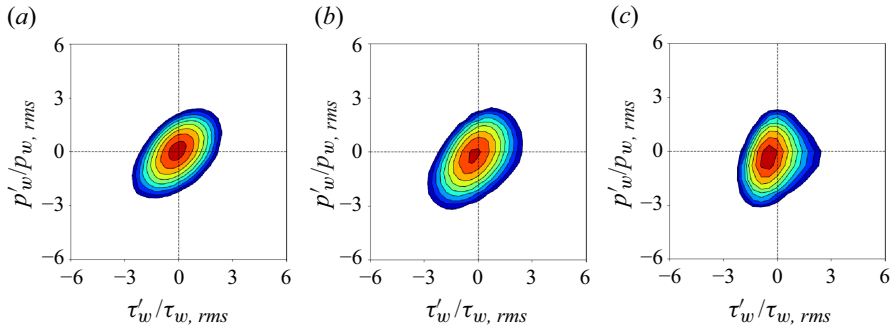


Figure 21. The JPDF of wall shear stress and pressure fluctuations at the inner wall, $P(\tau'_w, p'_w)$, for the R1 flow cases at $Re_b = 4000$ (a), 20 000 (b) and 87 000 (c).

and sweeps near the inner wall. A similar result was reported by Kuwata (2022) simulating a turbulent flow over high-aspect-ratio streamwise ribs, in which case the spanwise large-scale structures (originated by a Kelvin–Helmholtz instability) were found to increase locally pressure fluctuations and suppress the turbulent shear stress.

3.8. Role of spanwise structures on wall shear and pressure

Suppression of the turbulent shear stress associated with spanwise-coherent structures was found to yield frictional drag reduction by many authors (Koumoutsakos 1999; Fukagata, Kasagi & Sugiyama 2005; Mamori & Fukagata 2011). In addition, experiments on turbulent boundary layers revealed that characteristic and identifiable variation of the wall pressure accompanies the advection of large organised structures, which are responsible for variation of the wall shear stress (Thomas & Bull 1983). To understand whether spanwise large-scale structures play a role in reducing drag at the inner wall, we then investigate if strong pressure fluctuations due to the spanwise-coherent structures have a footprint on friction at the inner wall. For that purpose, we preliminarily verify whether those quantities are correlated by inspecting the joint probability density function (JPDF) of the wall shear stress and of the fluctuating pressure at the inner wall, which we report in figure 21. Strong positive correlation emerges at $Re_b = 4000$ (figure 21a) and $Re_b = 20\,000$ (figure 21b), at which flow near the inner wall is dominated by spanwise-coherent structures. This correlation becomes less distinct at $Re_b = 87\,000$ (figure 21c), at which turbulent fluctuations start reach down to the near-wall region. Hence, the effect of spanwise-coherent structures at the inner wall is to enhance pressure fluctuations, which are strongly correlated with shear stress fluctuations.

Strong fluctuations of the wall shear can contribute to friction reduction at the inner wall by increasing the number of backflow events. This insight is supported by the PDF of the wall shear stress reported in figure 22. The mildly curved cases, in which spanwise-coherent structures are not detected, can serve as a comparison. In addition, in table 2 we list the probability of backflow events. In the R40 flow cases (figure 22a) the PDFs of the wall shear stress at the inner and the outer wall are nearly identical, with increasing probability of large values of positive shear as the Reynolds number increases. Backflow events are very rare, with probability not exceeding 0.3%. The picture is quite different for the R1 flow cases (figure 22b). At the outer wall (solid lines), the probability of negative shear is lower than in the R40 flow cases. As evidenced by the increased probability of sweep motions on the concave wall (see § 3.9), we ascribe this backflow

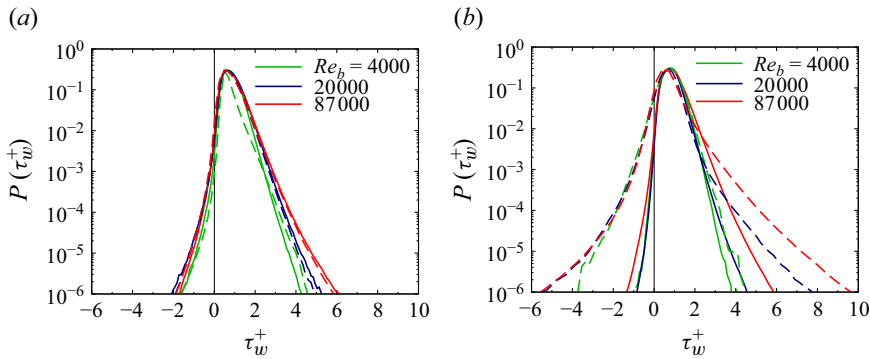


Figure 22. Probability density function (PDF) of the wall shear stress, $P(\tau_w^+)$, at various Reynolds numbers for flow cases R40 (a) and R1 flow cases (b). Dashed lines refer to the inner wall and solid lines refer to the outer wall.

inhibition to the strong secondary flow pushing high-speed fluid towards the wall. Hence, the flow on the concave side is less prone to separate, as backflow probability decreases with flow acceleration (Zaripov *et al.* 2023). A similar reduction in backflow events was observed in the outer bend of a toroidal pipe by Chin *et al.* (2020), who attributed it to a similar mechanism, suggesting an analogy between the effects of concave curvature and favourable pressure gradient. In contrast, the tails of the PDF widen at the inner wall (dashed lines), showcasing the amplification of wall-shear fluctuations induced by spanwise-coherent structures. The widening of the negative tail corresponds to an increase in backflow events at the inner wall, where their probability exceeds 4%.

Further insights into the relationship between wall pressure and wall shear are provided in figure 24, where we show the streamwise distribution of the coherent pressure and of the coherent shear stress at the inner wall, both normalised by their maximum value. Streamwise inhomogeneity induced by spanwise-coherent structures imposes a clear imprint on the wall pressure (blue lines), which features peaks and troughs corresponding to the high- and low-pressure regions observed in figure 19. The coherent wall shear stress (red lines) also features peaks and troughs, which we explain as follows. The coherent streamwise velocity of a clockwise-rotating roll cell (positive values of the stream function in figure 19) opposes the mean flow near the inner wall, reducing locally the streamwise velocity and hence the wall shear. Anticlockwise rotating roll cells act in the opposite way. The small-scale oscillations of the wall shear stress superposed to the large-scale ones at $Re_b = 87\,000$ (figure 22c) are due to turbulent activity, which explains reduced correlation between wall shear and wall pressure (see figure 21). The effects of spanwise-coherent structures on the flow field can be further characterised by analysing the phase shift between the wall shear stress and the wall pressure. The wavy pressure distribution generates local pressure gradients in the streamwise direction, which tend to accelerate and decelerate the fluid and result in alternating regions with high and low wall shear stress. Looking back at figure 19, one can see that high-pressure regions correspond to anticlockwise rotating eddies, and *vice versa* for the low-pressure regions. Hence, between any pair of counter-rotating eddies where the flow is locally subjected to an adverse pressure gradient ($u' < 0$) high-speed fluid is pushed towards the inner wall ($v' < 0$). Between any neighbouring pair, there is a favourable pressure gradient ($u' > 0$) and simultaneously low-speed fluid is diverted away from the inner wall ($v' > 0$). In both cases, the combination of these motions yields to $-u'v' < 0$, explaining why spanwise

Re_b	r_c/δ	$P(\tau_{w,i}^+ < 0)$	$P(\tau_{w,o}^+ < 0)$
4000	40.5	0.05	0.08
20 000	40.5	0.23	0.22
87 000	40.5	0.36	0.22
4000	1.0	4.38	0.10
20 000	1.0	3.92	0.09
87 000	1.0	4.50	0.16

Table 2. Probability of backflow events at the two walls at various Reynolds numbers, for the R40 ($r_c/\delta = 40.5$) and R1 ($r_c/\delta = 1$) flow cases.

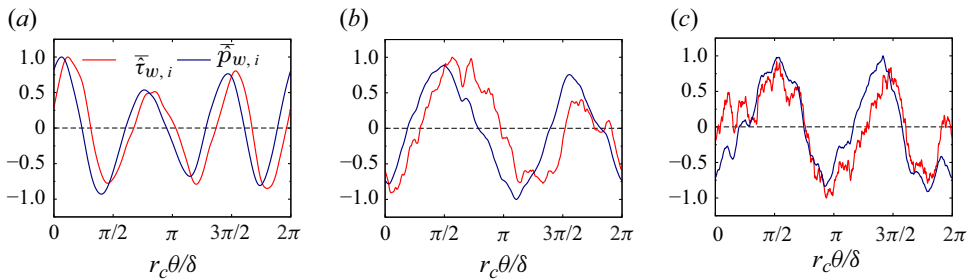


Figure 23. Streamwise distribution of mean coherent shear stress ($\bar{\tau}_{w,i}$, red lines), and mean coherent pressure ($\bar{p}_{w,i}$, blue lines) at the inner wall, for the R1 flow cases at $Re_b = 4000$ (a), 20 000 (b), 87 000 (c). Both quantities are normalised by their maximum value.

structures make a negative contribution to the production of Reynolds shear stress, which we have highlighted in figure 20(b).

3.9. Quadrant analysis

To provide a quantitative basis for the above analysis, we consider the JPDP of streamwise and wall-normal fluctuations, $P(u', v')$, defined such that

$$-\overline{u'v'} = \int_{-\infty}^{+\infty} u'v' P(u', v') du' dv', \tag{3.12}$$

where the covariance integrand, $u'v'P(u', v')$, is a measure of the contribution of each pair of u' and v' to the turbulent shear stress (Wallace & Brodkey 1977). Each quadrant of the (u', v') plane corresponds to a class of motions, specifically Q2 and Q4 quadrant events correspond to ‘ejections’ ($u' < 0$ and $v' > 0$) and ‘sweeps’ ($u' > 0$ and $v' < 0$), yielding positive contribution to the overall turbulent shear stress, whereas Q1 and Q3 quadrants correspond to ‘outward interactions’ ($u' > 0$ and $v' > 0$), and ‘inward interactions’ ($u' < 0$ and $v' < 0$), which yield negative contribution to it.

In figures 23 and 25 we show flooded contours of $P(u', v')$ superimposed to isolines of $u'v'P(u', v')$ for the R40 and R1 flow cases, respectively. The JPDP is evaluated in wall-parallel planes near the outer and the inner wall at $y^+ \approx 12$. In plane channel flow, this location is the ‘balance point’ where the contributions of ejections and sweeps are equal (Kim *et al.* 1987). In the R40 flow cases, the JPDP at the outer wall (figures 23a–c and 25a–c) has a roughly elliptical shape with major axis inclined along the Q2 and

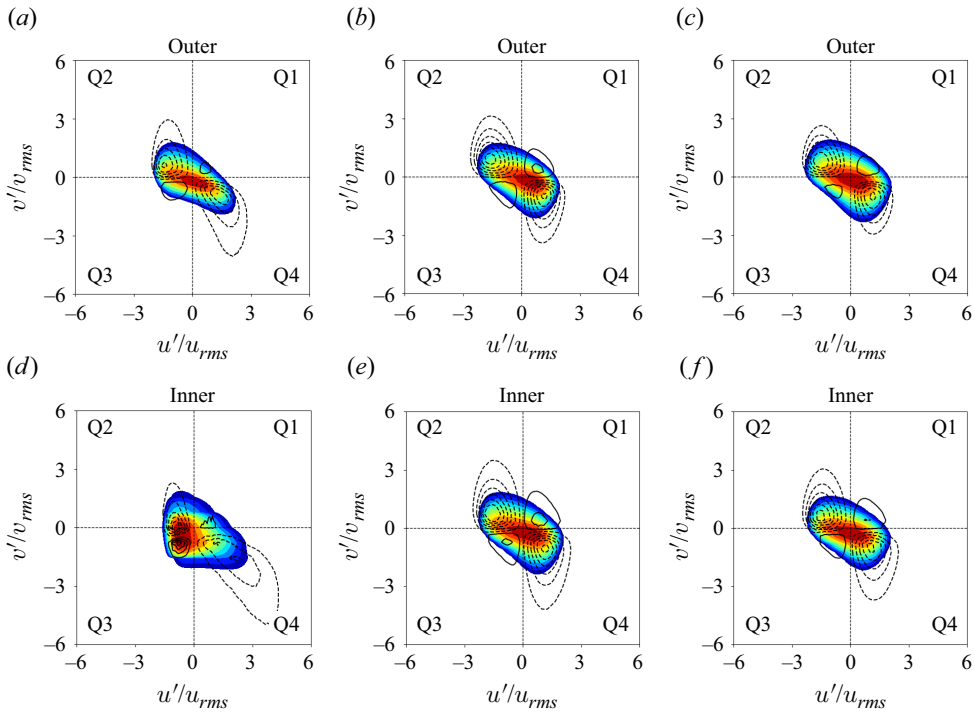


Figure 24. The JPDF of streamwise and wall-normal velocity fluctuations, superimposed to flooded contours of the covariance integrand, near the outer wall (*a–c*) and the inner wall (*d–f*) at $y^+ \approx 12$, for the R1 flow cases. The panels correspond to $Re_b = 4000$ (*a,d*), 20 000 (*b,e*), 87 000 (*c,f*).

Q4 quadrants, pointing to high probability of sweeps and ejections. Similar observations apply to the fully turbulent R40 flow cases near the inner wall (figure 25*e,f*), and also for the R1 flow cases near the outer wall (figure 23*a–c*). However, strong curvature seems to increase the probability of sweeps more than ejections, which can be inferred from the shift of the JPDF peak towards the Q4 quadrant. As previously noted, this tendency is associated with strong secondary motions that transport high-velocity fluid from the channel core towards the outer wall, increasing near-wall velocity and thereby suppressing the formation of regions with negative velocity (see figure 22). The scenario is different at the inner wall. In the R40 flow case at $Re_b = 4000$, as depicted in figure 25(*d*), the peak probability is mainly concentrated in the Q2 and Q3 quadrants, and to a lesser extent in the Q4 quadrant, on account of stronger, less probable values of u' and v' . The roughly circular shape of the JPDF at the inner wall in the R1 flow cases (figure 23*d–f*) points to the suppression of the negative correlation between u' and v' which is typical of near-wall turbulent flow. In addition, the covariance integrand highlights that the contribution to the turbulent stress is not dominated by the Q2 and Q4 motions, but rather strong contributions also come from Q1 and Q3 motions.

The same results are quantified in table 3, where we list the integrated contributions to the turbulent shear stress from each quadrant, at $y^+ \approx 12$. For the R40 fully turbulent flow cases the results are comparable to experimental results for plane channel flow (Wallace, Eckelmann & Brodkey 1972), namely the contribution of both ejections and sweeps is approximately 70 %, whereas inward and outward interactions each contribute negatively by approximately 20 %. At $Re_b = 4000$, the Q2 contribution near the inner wall reduces

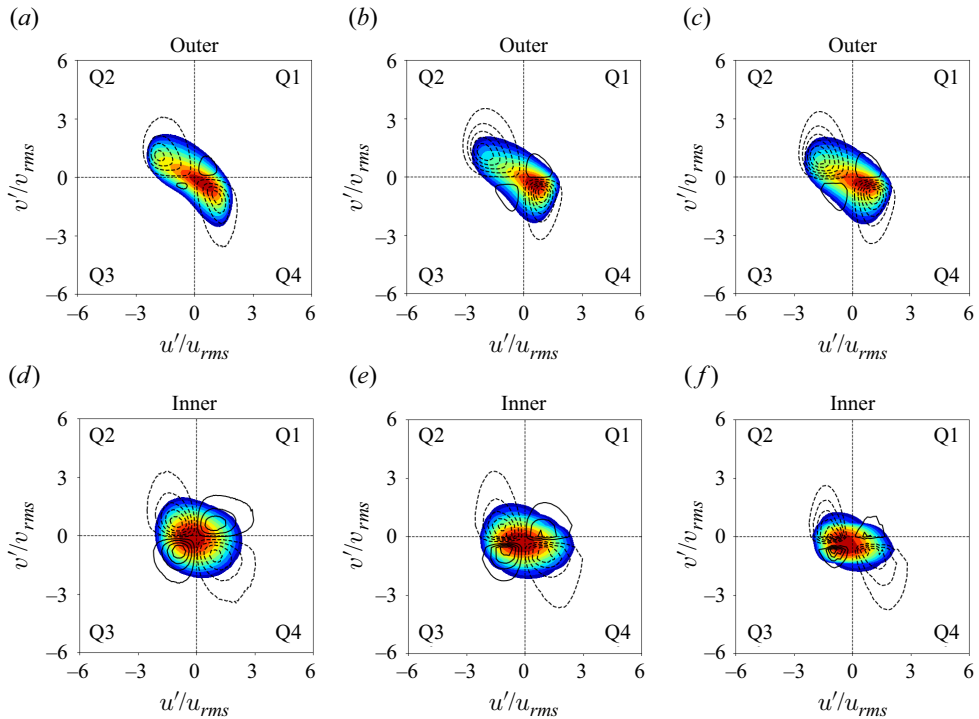


Figure 25. The JPDF of streamwise and wall-normal velocity fluctuations, superimposed to flooded contours of the covariance integrand, near the outer wall (a–c) and near the inner wall (d–f) at $y^+ \approx 12$, for the R40 flow cases. These panels correspond to $Re_b = 4000$ (a,d), 20 000 (b,e), 87 000 (c,f).

to 30 %, which is comparable to the Q1 contribution but opposite in sign, whereas the Q4 contribution exceeds 110 % of the shear stress. Combining this value with the shape of the JPDF in figure 25(d), one can infer that larger, energetic but infrequent motions are the main contributors to the turbulent shear stress. These strong sweeps can be attributed to the streamwise vortices pushing the high-speed mean flow from the channel core towards the inner wall. As for the R1 flow cases, the quadrant contributions at the outer wall are similar to those of the R40 flow cases, except for greater contribution of ejections as compared with sweeps. Hence, the most probable motions (i.e. sweeps, as visible in figure 23) do not contribute as much to the turbulent shear stress as the ejections, see table 3. At the inner wall, the fractional contributions of the outward (Q1) and inward (Q3) interactions exceeds half the contributions of ejections (Q2) and sweeps (Q4). This result confirms that the spanwise large-scale structures, which were found to generate Q1 and Q3 motions in § 3.8, dampen the turbulent shear stress on the convex side of strongly curved channels.

3.10. Energy production reversal

The Q1 and Q3 motions contribute negatively to turbulent shear stress, hence they yield negative contribution to the production of TKE, $\mathcal{P} = -\overline{u'v'}$ \mathcal{S} , where $\mathcal{S} = dU/dr - U/r$ is the mean shear rate. Based on the analysis in § 3.9, we expect that TKE production be reduced near the inner wall in flow cases with strong curvature. In figure 26(a) we then show the TKE production for the R1 flow cases. Near the outer wall (solid lines) all

Re_b	Q1	Q2	Q3	Q4
		R40 outer wall		
4000	-8.90	+47.56	-7.90	+69.24
20 000	-12.67	+66.64	-10.10	+56.13
87 000	-16.60	+66.59	-11.63	+61.64
		R40 inner wall		
4000	-30.76	+31.38	-11.82	+111.19
20 000	-14.10	+63.82	-9.57	+59.86
87 000	-17.26	+63.75	-10.81	+64.33
		R1 outer wall		
4000	-5.09	+56.27	-2.43	+51.29
20 000	-7.01	+72.47	-7.09	+41.64
87 000	-9.58	+68.95	-9.51	+50.14
		R1 inner wall		
4000	-75.25	+115.39	-65.18	+125.04
20 000	-60.01	+95.88	-49.38	+113.52
87 000	-39.40	+59.72	-21.18	+100.86

Table 3. Percent contribution of quadrants to turbulent shear stress ($\overline{u'v'} Q_i / \overline{u'v'}$), for the R40 and R1 flow cases near the inner and outer wall, at $y^+ \approx 12$.

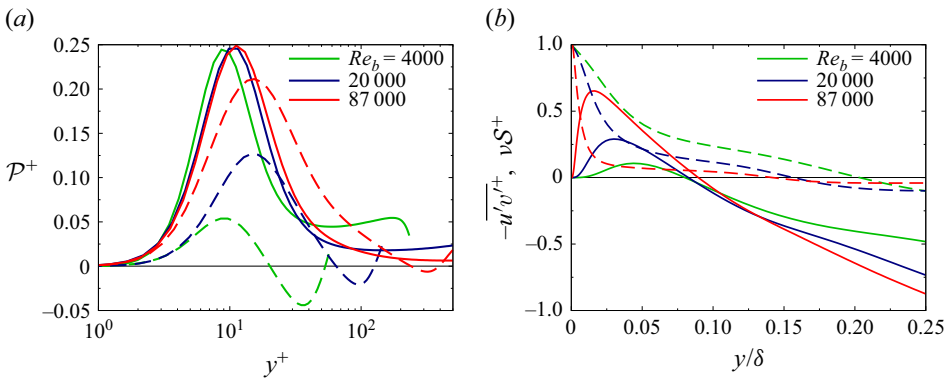


Figure 26. (a) The TKE production (P^+) near the outer wall (solid lines) and near the inner wall (dashed lines). (b) Turbulent shear stress ($-\overline{u'v'}^+$, solid lines) and viscous shear stress (νS^+ , dashed lines) near the inner wall. All quantities are reported in local wall units for the R1 flow cases.

distributions tend to collapse, especially at high Reynolds number, revealing that the flow similarity is preserved near the outer wall. The peak production is located at $y^+ \approx 12$ (except at $Re_b = 4000$, for which the peak occurs at $y^+ \approx 9$) and the peak value is $P^+ \approx 0.25$, similar to plane channel flow (Kim *et al.* 1987; Laadhari 2002). In contrast, TKE production near the inner wall (dashed lines) depends heavily on the Reynolds number, implying that classical wall scaling no longer holds near highly convex surfaces. Notably, a region appears where the production is negative, with an extent of 0.12δ at $Re_b = 4000$ and gradually reducing at higher Reynolds numbers. For the production to be positive everywhere, the turbulent shear stress and the viscous shear stress must have the same sign and vanish at the same location. This is not the case for the strongly curved channel, as clearly illustrated in figure 26(b), which shows profiles of the turbulent shear

stress, $-\overline{u'v'^+}$ (solid lines), and of the viscous shear stress, $\nu\mathcal{S}^+$ (dashed lines), near the inner wall in the R1 flow cases. The displacement between the zero-crossings of the turbulent shear stress and of the viscous shear is related to asymmetry of the mean velocity profile (Beguier *et al.* 2005) and leads to a region of opposing shear where $-\overline{u'v'^+} < 0$ and $\nu\mathcal{S}^+ > 0$, hence $\mathcal{P}^+ < 0$.

As pointed out in § 3.1, the zero crossing of the mean shear marks the interface between the two distinct flow structures developing at each wall. Straddling this interface there is a diffusive transfer of shear stress from the outer- to the inner-wall region that has a sign opposite to the locally produced shear stress, leading to negative net TKE production (Hanjalić & Launder 1972). In the region with negative production local energy reversal takes place, whereby energy is transferred from turbulent fluctuations to the mean flow (Eskinazi & Erian 1969). Besides its physical significance, this result provides useful caveat for use of RANS models for simulations of turbulent flows over convex walls. In fact, standard eddy-viscosity models would clearly fail if turbulent shear stress and mean shear do not go to zero at the same location.

4. Conclusions

We have investigated fully developed flow in a curved channel to get insight into turbulence bounded by curved walls. This set-up showcases rich physics due to the interplay of fine-scale turbulence with large-scale coherent structures driven by centrifugal instabilities, which break the symmetry of the flow resulting in distinctly different behaviour near convex and concave walls. We have focused on the effects of curvature by examining two extreme cases, a mildly curved channel with radius of curvature $r_c/\delta = 40.5$ and a strongly curved channel with $r_c/\delta = 1$, with δ the channel height. For each geometry, we have studied the effect of Reynolds number (Re_b) through an extensive series of DNS, covering flow regimes from laminar up to the moderately high value of $Re_b = u_b\delta/\nu = 87\,000$, where u_b is the bulk velocity and ν the kinematic viscosity. Our analysis has shown that in laminar flow the friction coefficient is higher at the convex wall, whereas the opposite holds in the turbulent regime. Flow transition is anticipated by concave curvature and delayed by convex curvature, thus preventing turbulence to fully develop near the inner wall of strongly curved channels. For mild curvature, the global friction based on the mean-pressure gradient is less than in plane channel flow at the same flow rate within the range of ‘transitional’ Reynolds numbers $3000 \leq Re_b \leq 10\,000$, with a maximum frictional drag reduction of 12.2% at $Re_b = 4000$. This behaviour is not observed in strongly curved channels, for which friction is higher than the planar case in the transitional regime, and becomes roughly equivalent at $Re_b \geq 40\,000$. Through spectral analysis and flow field visualisations, we managed to detect the typical hallmarks of the near-wall turbulence regeneration cycle at both walls in the case of mild curvature, whereas wall turbulence is virtually suppressed on the convex side of strongly curved channels. Clear footprints of streamwise- and spanwise-aligned large-scale structures were also found.

Streamwise large-scale structures, originating from centrifugal instabilities and reminiscent of the Dean vortices found in laminar flow, were identified through an eduction scheme based on triple decomposition, which also allowed us to quantify their effects on turbulence. Specifically, streamwise coherent structures were found to depend weakly on Reynolds number and highly on the channel geometry. In case of mild curvature, streamwise vortices modify the spanwise distribution of the wall shear and contribute significantly to streamwise velocity fluctuations and turbulent shear stress, consistent with

previous studies. For strong curvature, these vortices are displaced towards the outer wall, becoming smaller in size and less stable, as we have shown by combined use of spectral analysis and triple decomposition. As a consequence, the impact of streamwise roll cells on the wall shear and momentum transfer is marginal, whereas the wall-normal velocity is strongly affected.

Spanwise-aligned large-scale structures were also observed on the convex side of strongly curved channels, leaving a footprint characterised by pressure disturbances being advected downstream at approximately the mean flow speed. These structures were analysed using triple decomposition and phase averaging, revealing their role in amplifying pressure disturbances. This amplification correlates with large fluctuations of the wall shear stress, which may contribute to friction reduction. The link between enhanced pressure fluctuations and reduced wall friction is ascribed to the generation of alternating favourable and adverse pressure gradients. These gradients interact with upward and downward radial motions, respectively, leading to suppression of the turbulent shear stress near the convex wall. This mechanism was further investigated and quantified through quadrant analysis of streamwise and wall-normal velocity fluctuations, which highlighted enhancement of inward and outward interactions (i.e. Q3 and Q1 motions), resulting in the emergence of a region with negative turbulence production. The reduction in size of streamwise vortices and the onset of spanwise structures – specific to strongly curved channels and not observed in previous studies – suggest that the flow physics undergo substantial changes when the curvature exceeds a critical threshold. Further study encompassing a wider range of relative curvature is required to determine the exact value at which these changes take place and the coherence of near-wall streaks on the inner wall breaks down.

These results offer valuable information regarding the fundamental physics of flows over curved walls, as well as for turbulence modelling, e.g. subgrid-scale models for LES and RANS closures. We also believe that insights gained from analysis of curved channel flow in a temporal setting may be relevant to understanding the case of spatially developing boundary layers over convex and concave surfaces. In fact, our analysis has shown that the interaction between the inner- and outer-wall regions is concentrated in the channel core, whereas the inner-wall (outer-wall) region is dominated by convex (concave) curvature effects.

Acknowledgements. The results reported in this paper have been achieved using the EuroHPC Research Infrastructure resource LEONARDO based at CINECA, Casalecchio di Reno, Italy, under project EuroHPC 02044 and IscraB CONCORDE.

Funding. This research received financial support from ICSC-Centro Nazionale di Ricerca in ‘High Performance Computing, Big Data and Quantum Computing’, funded by European Union-NextGenerationEU.

Declaration of interests. The authors report no conflict of interest.

Data availability statement. All data that support the findings of this study are available from the corresponding author upon request.

A. Effects of domain size

Six additional simulations have been carried out to verify *a posteriori* the adequacy of the domain sizes used in the DNS campaign. Here, we consider the Reynolds number $Re_b = 5000$, which is the least to have fully turbulent flow. As for the R40 flow cases, from the baseline configuration ($L_\theta/\delta = 2\pi$, $L_z/\delta = 4$) we have doubled and quadrupled both L_θ (for fixed L_z) and L_z (for fixed L_θ), by retaining the same grid spacing. As

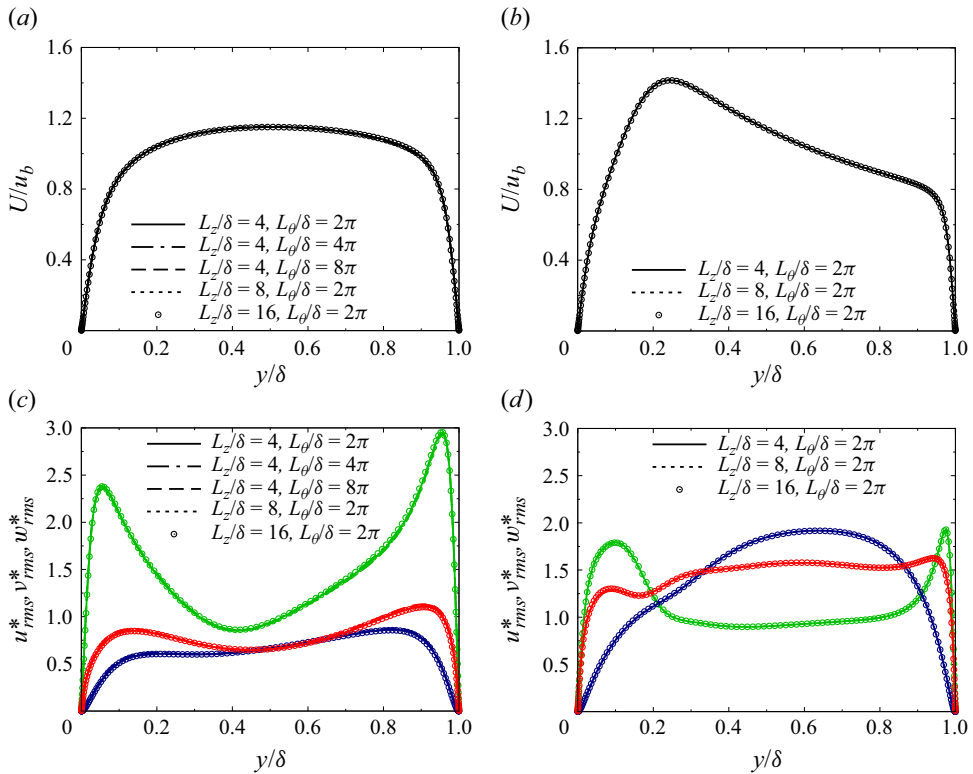


Figure 27. Mean streamwise velocity (U/u_b) for the R40 flow cases (a) and R1 flow cases (b); r.m.s. profiles of streamwise (green), wall-normal (blue) and spanwise (red) velocity fluctuations for the R40 flow cases (c) and R1 flow cases (d). The Reynolds number is fixed at $Re_b = 5000$ and the domain size is varied as marked, case by case, by the different line types.

for the R1 flow cases, the streamwise extent of the domain covers a full circumference, hence it was not increased. From $L_z/\delta = 8$ used in the baseline DNS, the spanwise extent was decreased to $L_z/\delta = 4$ and increased to $L_z/\delta = 16$. In figure 27 we show the mean streamwise velocity (figure 27a,b) and the r.m.s. profiles of streamwise (green), wall-normal (blue) and spanwise (red) velocity fluctuations (figure 27c,d) for both the R40 flow cases (figure 27a,c) and R1 flow cases figure 27(b,d). One will see that all the profiles obtained with the different combinations of domain size (marked by the different line types) nearly collapse to a single line, showing that the domain size used in the DNS campaign is adequate.

B. Global friction velocity

The derivation of the global friction velocity has been shown by Brethouwer (2022) starting from the mean momentum balance, yet we believe that it may be instructive to illustrate briefly how it relates to the mean-pressure gradient. The analytical expression of the streamwise pressure gradient as a function of the shear stresses at the two walls can be derived in the simplest way from the balance of moments of forces about the centre of curvature, which, referring to the sketch of figure 28, reads

$$\int_{r_i}^{r_o} \left(-P - \frac{\partial P}{\partial \theta} \Delta\theta + P \right) r dr + \left(\tau_{w,i} r_i^2 + \tau_{w,o} r_o^2 \right) \Delta\theta = 0. \quad (B1)$$

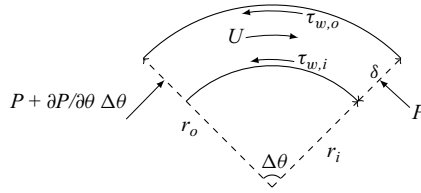


Figure 28. Sketch of the curved channel flow.

Hence, recalling that $r_c = (r_o + r_i)/2$ and $\delta = r_o - r_i$, we obtain

$$-\frac{dP}{d\theta} = \frac{\tau_{w,i}r_i^2 + \tau_{w,o}r_o^2}{r_c\delta}. \tag{B2}$$

To define a global friction velocity, $u_{\tau,g}$, an equivalent length of the curved channel must be defined. Considering the length of the channel at the centreline, $L_\theta = r_c\Delta\theta$, one obtains

$$-\frac{1}{\rho r_c} \frac{dP}{d\theta} = 2 \frac{u_{\tau,g}^2}{\delta} \Rightarrow u_{\tau,g}^2 = \frac{u_{\tau,i}^2 r_i^2 + u_{\tau,o}^2 r_o^2}{2r_c^2} \tag{B3}$$

where $u_{\tau,i}^2 = \tau_{w,i}/\rho$ and $u_{\tau,o}^2 = \tau_{w,o}/\rho$.

C. Convergence of flow statistics

Whether the statistics are well-converged can be verified by comparing the analytical profile of the total shear stress with the DNS results. As shown by Brethouwer (2022), starting from the mean momentum equation in streamwise direction for the curved channel flow, which reads

$$0 = -\frac{1}{\rho r} \frac{\partial P}{\partial \theta} + \nu \left(\frac{1}{r} \frac{\partial U}{\partial r} - \frac{U}{r^2} + \frac{\partial^2 U}{\partial r^2} \right) - \left(\frac{\partial \overline{uv}}{\partial r} + \frac{2}{r} \overline{uv} \right), \tag{C1}$$

one can derive the following equation for the total shear stress distribution

$$\tau(r) = \frac{r_i^2 \tau_{w,i} (r_o^2 - r^2) + r_o^2 \tau_{w,o} (r_i^2 - r^2)}{2r^2 r_c \delta}. \tag{C2}$$

In figure 29 we show the analytical profile of the total shear stress (circles) and the DNS results at the corresponding Reynolds numbers (solid lines). The DNS results effectively collapse to the analytical profile, which corroborates that satisfactory statistical convergence is achieved.

D. Assessment of the triple decomposition

The streamwise large-scale vortices are not necessarily coherent over the entire extent of the domain, and unsteady splitting and merging events may also take place (see § 3.5). Consequently, the coherent contribution from the streamwise vortices defined in (3.6) would approach zero as the domain length (L_θ) approaches infinity. This effect is illustrated in figure 30(a), where the r.m.s. profiles of coherent streamwise velocity (\tilde{u}_{rms}^*) are plotted for the R40 flow case at $Re_b = 10\,000$, using different values of L_θ . As expected, the intensity of coherent fluctuations decreases for longer domains.

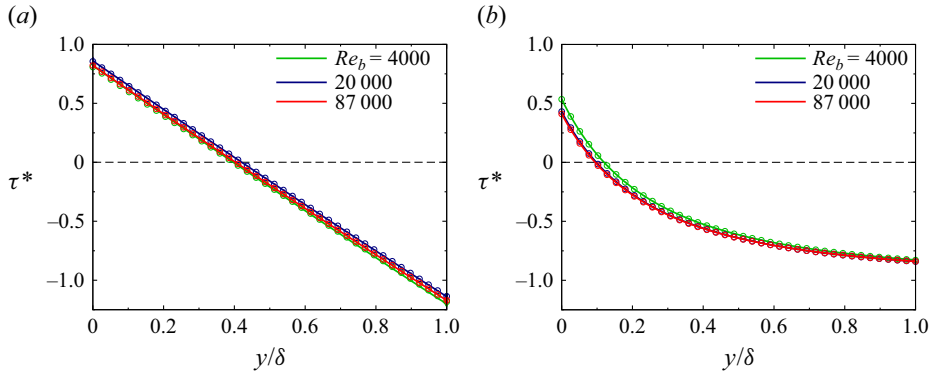


Figure 29. Mean profile of the total shear stress (τ^*) at various Reynolds numbers for the R40 flow cases (a) and R1 flow cases (b). Circles denote the analytical profile (C2).

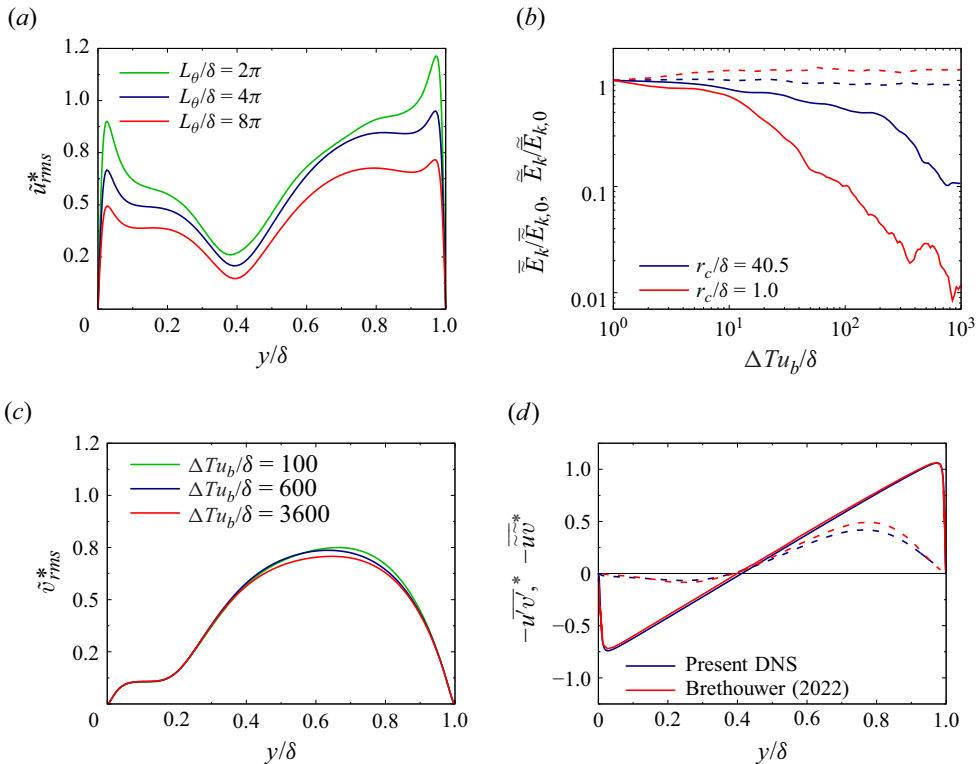


Figure 30. (a) The r.m.s. profiles of coherent streamwise velocity fluctuations for the R40 flow case at $Re_b = 10\,000$ for various domain lengths. (b) Kinetic energy of time-averaged coherent motions (solid lines) and time-averaged kinetic energy of coherent motions (dashed lines) scaled by the initial value as a function of the averaging time period. (c) The r.m.s. profiles of coherent wall-normal velocity fluctuations for the R1 flow case at $Re_b = 10\,000$ for various averaging periods. (d) Total (solid lines) and coherent (dashed lines) turbulent shear stress for the R40 flow case at $Re_b = 40\,000$, compared with the results obtained by Brethouwer (2022) for $r_c/\delta = 30$ at $Re_b = 40\,000$.

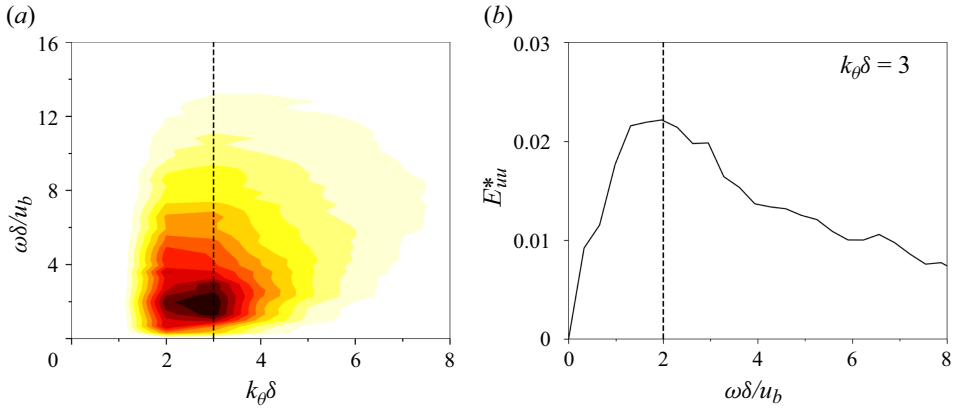


Figure 31. (a) Wavenumber-frequency spectra of the fluctuating streamwise velocity, $E_{uu}^*(k_\theta, \omega)$, for the R1 flow case at $Re_b = 4000$; (b) $E_{uu}^*(\omega)$ at $k_\theta \delta = 3$. The wall distance is fixed at $y/\delta = 0.09$.

Another aspect to take into account is that the streamwise vortices are free to move in the spanwise direction, whereby the time-averaged coherent contribution would approach zero as the averaging period (T) approaches infinity. This effect is assessed in figure 30(b), where we show the kinetic energy associated with the time-averaged coherent motions, defined as $\overline{\tilde{E}}_k = \langle (\overline{\tilde{u}^2} + \overline{\tilde{v}^2} + \overline{\tilde{w}^2})/2 \rangle_{r,z}$ as a function of T (solid lines). The time-averaging is carried out over incremental time periods from $T = 1\delta/u_b$ to $T = 1000\delta/u_b$. The temporal decay of $\overline{\tilde{E}}_k$ is evident, occurring more rapidly in the R1 flow case due to increased unsteadiness of streamwise vortices. However, the time-averaged kinetic energy of coherent motions, defined as $\overline{\tilde{E}}_k = \overline{(\tilde{u}^2 + \tilde{v}^2 + \tilde{w}^2)/2}_{r,z}$ is nearly constant for increasing T (dashed lines), implying that the variance of (3.6) is independent of the averaging period. The same conclusion can be drawn from figure 30(c), which shows the r.m.s. profiles of coherent wall-normal velocity (\tilde{v}_{rms}^*) for the R1 flow case at $Re_b = 10000$. All profiles, obtained using different values of T , are nearly overlapping.

The present results obtained with $L_\theta = 2\pi\delta$ for the R40 flow case at $Re_b = 40\,000$ are compared with those reported in Brethouwer (2022) for the flow in a curved channel with similar wall curvature ($r_c/\delta = 30$) at the same Reynolds number. As shown in figure 30(d), the profiles of the turbulent shear stress are virtually overlapping (solid lines) and, despite the curvature is not identical, the coherent contribution is comparable (dashed lines).

E. Estimation of the convection velocity

In figure 31(a) we show the wavenumber-frequency spectra of the streamwise velocity fluctuations, $E_{uu}^*(k_\theta, \omega)$, for the R1 flow case at $Re_b = 4000$. The wall distance is kept fixed at $y/\delta = 0.09$, which is the peak location of $k_\theta^* E_{uu}^*$ related to spanwise structures (see figure 11). An energy peak appears in the spectral density at the wavenumber $k_\theta \delta \approx 3$ (marked by the vertical dashed line) corresponding to $\lambda_\theta/\delta \approx 2\pi/3$, which is the wavelength of spanwise structures at $Re_b = 4000$ (see figure 11). As seen in figure 31(b), showing $E_{uu}^*(\omega)$ fixed the wavenumber at $k_\theta \delta = 3$, the energy peak is at the angular frequency $\omega \approx 2u_b/\delta$. Hence, the convection velocity of spanwise structures can be estimated as $u_c = \omega/k_\theta \approx 0.67u_b$.

REFERENCES

- ALFREDSSON, P.H. & PERSSON, H. 1989 Instabilities in channel flow with system rotation. *J. Fluid Mech.* **202**, 543–557.
- BEGUIER, C., GIRALT, F., FULACHIER, L. & KEFFER, J.F. 2005 Negative production in turbulent shear flows. In *Structure and Mechanisms of Turbulence II*, pp. 22–35. Springer.
- BRADSHAW, P. & YOUNG, A.D. 1973 The effects of streamline curvature on turbulent flow. Tech. Report AGARD-AG-169. Advisory Group for Aerospace Research and Development Paris.
- BRETHOUWER, G. 2017 Statistics and structure of spanwise rotating turbulent channel flow at moderate Reynolds numbers. *J. Fluid Mech.* **828**, 424–458.
- BRETHOUWER, G. 2022 Turbulent flow in curved channels. *J. Fluid Mech.* **931**, A21.
- BREWSTER, D.B., GROSBURG, P. & NISSAN, A.H. 1959 The stability of viscous flow between horizontal concentric cylinders. *Proc. R. Soc. Lond. A* **251** (1264), 76–91.
- CANTON, J., ÖRLÜ, R., CHIN, C., HUTCHINS, N., MONTY, J. & SCHLATTER, P. 2016 On large-scale friction control in turbulent wall flow in low Reynolds number channels. *Flow Turbul. Combust.* **97** (3), 811–827.
- CHIN, R.C., VINUESA, R., ÖRLÜ, R., CARDESA, J.I., NOORANI, A., CHONG, M.S. & SCHLATTER, P. 2020 Backflow events under the effect of secondary flow of Prandtl's first kind. *Phys. Rev. Fluids* **5** (7), 074606.
- CHO, M., HWANG, Y. & CHOI, H. 2018 Scale interactions and spectral energy transfer in turbulent channel flow. *J. Fluid Mech.* **854**, 474–504.
- DAI, Y.J., HUANG, W.X. & XU, C.X. 2016 Effects of Taylor-Görtler vortices on turbulent flows in a spanwise-rotating channel. *Phys. Fluids* **28** (11).
- DEAN, W.R. 1928 Fluid motion in a curved channel. *Proc. R. Soc. Lond. A* **121** (787), 402–420.
- ECKHAUS, W. 1965 *Studies in Non-Linear Stability Theory*. Springer.
- ELLIS, L.B. & JOUBERT, P.N. 1974 Turbulent shear flow in a curved duct. *J. Fluid Mech.* **62** (1), 65–84.
- ESKINAZI, S. & ERIAN, F.F. 1969 Energy reversal in turbulent flows. *Phys. Fluids* **12** (10), 1988–1998.
- ESKINAZI, S. & YEH, H. 1956 An investigation on fully developed turbulent flows in a curved channel. *J. Aeronaut. Sci.* **23** (1), 23–34.
- FINLAY, W.H., KELLER, J.B. & FERZIGER, J.H. 1988 Instability and transition in curved channel flow. *J. Fluid Mech.* **194** (1), 417–456.
- FUKAGATA, K., KASAGI, N. & SUGIYAMA, K. 2005 Feedback control achieving sublamina friction drag. In *Proceedings of the 6th Symposium on Smart Control of Turbulence*, pp. 143–148.
- GILLIS, J.C. & JOHNSTON, J.P. 1983 Turbulent boundary-layer flow and structure on a convex wall and its redevelopment on a flat wall. *J. Fluid Mech.* **135** (1), 123–153.
- GUO, Y. & FINLAY, W.H. 1991 Splitting, merging and wavelength selection of vortices in curved and/or rotating channel flow due to Eckhaus instability. *J. Fluid Mech.* **228**, 661–691.
- HAMILTON, J.M., KIM, J. & WALEFFE, F. 1995 Regeneration mechanisms of near-wall turbulent structures. *J. Fluid Mech.* **287**, 317–348.
- HANJALIĆ, K. & LAUNDER, B.E. 1972 Fully developed asymmetric flow in a plane channel. *J. Fluid Mech.* **51** (2), 301–335.
- HARLOW, F.H. & WELCH, J.E. 1965 Numerical calculation of time-dependent viscous incompressible flow of fluid with free surface. *Phys. Fluids* **8** (12), 2182–2189.
- HUNT, I.A. & JOUBERT, P.N. 1979 Effects of small streamline curvature on turbulent duct flow. *J. Fluid Mech.* **91** (4), 633–659.
- HUSSAIN, A.K.M.F. 1986 Coherent structures and turbulence. *J. Fluid Mech.* **173**, 303–356.
- HUSSAIN, A.K.M.F. & REYNOLDS, W.C. 1970 The mechanics of an organized wave in turbulent shear flow. *J. Fluid Mech.* **41** (2), 241–258.
- JIMENEZ, J., UHLMANN, M., PINELLI, A. & KAWAHARA, G. 2001 Turbulent shear flow over active and passive porous surfaces. *J. Fluid Mech.* **442**, 89–117.
- KIM, J. & HUSSAIN, F. 1993 Propagation velocity of perturbations in turbulent channel flow. *Phys. Fluids A: Fluid Dyn.* **5** (3), 695–706.
- KIM, J., MOIN, P. & MOSER, R.D. 1987 Turbulence statistics in fully developed channel flow at low Reynolds number. *J. Fluid Mech.* **177**, 133–166.
- KOBAYASHI, M., MAEKAWA, H., TAKANO, T., UCHIYAMA, N., KUBOTA, M. & KOBAYASHI, Y. 1989 Two-dimensional turbulent flow in a curved channel. *JSME Intl J. Ser.* **32** (3), 324–331.
- KOUMOUTSAKOS, P. 1999 Vorticity flux control for a turbulent channel flow. *Phys. Fluids* **11** (2), 248–250.
- KRISTOFFERSEN, R. & ANDERSSON, H.I. 1993 Direct simulations of low-Reynolds-number turbulent flow in a rotating channel. *J. Fluid Mech.* **256**, 163–197.
- KUWATA, Y. 2022 Dissimilar turbulent heat transfer enhancement by Kelvin–Helmholtz rollers over high-aspect-ratio longitudinal ribs. *J. Fluid Mech.* **952**, A21.
- LAADHARI, F. 2002 On the evolution of maximum turbulent kinetic energy production in a channel flow. *Phys. Fluids* **14** (10), L65–L68.

- LE CUNFF, C. & BOTTARO, A. 1993 Linear stability of shear profiles and relation to the secondary instability of the dean flow. *Phys. Fluids A: Fluid Dyn.* **5** (9), 2161–2171.
- LEE, M. & MOSER, R.D. 2015 Direct numerical simulation of turbulent channel flow up to $Re_\tau \approx 5200$. *J. Fluid Mech.* **774**, 395–415.
- LIGRANI, P.M., LONGEST, J.E., KENDALL, M.R. & FIELDS, W.A. 1994 Splitting, merging and spanwise wavenumber selection of dean vortex pairs. *Exp. Fluids* **18** (1-2), 41–58.
- LIGRANI, P.M. & NIVER, R.D. 1988 Flow visualization of dean vortices in a curved channel with 40 to 1 aspect ratio. *Phys. Fluids* **31** (12), 3605–3617.
- MAMORI, H. & FUKAGATA, K. 2011 Drag reduction by streamwise traveling wave-like Lorenz force in channel flow. *J. Phys.: Conf. Ser.* **318** (2), 022030.
- MAMORIN, O.J.E. & ALFREDSSON, P.H. 1990 Curvature- and rotation-induced instabilities in channel flow. *J. Fluid Mech.* **210**, 537–563.
- MAMORIN, O.J.E. & ALFREDSSON, P.H. 1992 Experiments on instabilities in curved channel flow. *Phys. Fluids A: Fluid Dyn.* **4** (8), 1666–1676.
- MATSUBARA, K. & MIURA, T. 2017 Spatially advancing turbulent flow and heat transfer in a curved channel at friction-velocity-based Reynolds number 550. *Intl J. Heat Mass Transfer* **108**, 2433–2443.
- MONTY, J.P., HUTCHINS, N., NG, H.C.H., MARUSIC, I. & CHONG, M.S. 2009 A comparison of turbulent pipe, channel and boundary layer flows. *J. Fluid Mech.* **632**, 431–442.
- MOSER, R.D. & MOIN, P. 1987 The effects of curvature in wall-bounded turbulent flows. *J. Fluid Mech.* **175** (1), 479–510.
- NAGATA, M. & KASAGI, N. 2004 Spatio-temporal evolution of coherent vortices in wall turbulence with streamwise curvature. *J. Turbul.* **5** (1), 017.
- ORLANDI, P., BERNARDINI, M. & PIROZZOLI, S. 2015 Poiseuille and Couette flows in the transitional and fully turbulent regime. *J. Fluid Mech.* **770**, 424–441.
- ORLANDI, P. & FATICA, M. 1997 Direct simulations of turbulent flow in a pipe rotating about its axis. *J. Fluid Mech.* **343**, 43–72.
- PATEL, V.C. & HEAD, M.R. 1969 Some observations on skin friction and velocity profiles in fully developed pipe and channel flows. *J. Fluid Mech.* **38** (1), 181–201.
- PIROZZOLI, S. 2023 Searching for the log law in open channel flow. *J. Fluid Mech.* **971**, A15.
- PIROZZOLI, S., ROMERO, J., FATICA, M., VERZICCO, R. & ORLANDI, P. 2021 One-point statistics for turbulent pipe flow up to $Re_\tau \approx 6000$. *J. Fluid Mech.* **926**, A28.
- RAMAPRIAN, B.R. & SHIVAPRASAD, B.G. 1978 The structure of turbulent boundary layers along mildly curved surfaces. *J. Fluid Mech.* **85** (2), 273–303.
- RAYLEIGH, J.W.S. 1917 On the dynamics of revolving fluids. *Proc. R. Soc. Lond. A* **93** (648), 148–154.
- SO, R.M.C. & MELLOR, G.L. 1973 Experiment on convex curvature effects in turbulent boundary layers. *J. Fluid Mech.* **60** (1), 43–62.
- TAYLOR, G.I. 1923 Stability of a viscous liquid contained between two rotating cylinders. *Phil. Trans. R. Soc. Lond. A* **223**, 289–343.
- THOMAS, A.S.W. & BULL, M.K. 1983 On the role of wall-pressure fluctuations in deterministic motions in the turbulent boundary layer. *J. Fluid Mech.* **128** (-1), 283–322.
- VERZICCO, R. & ORLANDI, P. 1996 A finite-difference scheme for three-dimensional incompressible flows in cylindrical coordinates. *J. Comput. Phys.* **123** (2), 402–414.
- WALLACE, J.M. & BRODKEY, R.S. 1977 Reynolds stress and joint probability density distributions in the $u - v$ plane of a turbulent channel flow. *Phys. Fluids* **20** (3), 351–355.
- WALLACE, J.M., ECKELMANN, H. & BRODKEY, R.S. 1972 The wall region in turbulent shear flow. *J. Fluid Mech.* **54** (1), 39–48.
- WATTENDORF, F.L. 1935 A study of the effect of curvature on fully developed turbulent flow. *Proc. R. Soc. Lond. A* **148** (865), 565–598.
- YANG, Y.T. & WU, J.Z. 2012 Channel turbulence with spanwise rotation studied using helical wave decomposition. *J. Fluid Mech.* **692**, 137–152.
- YIMPRASERT, S., KVICK, M., ALFREDSSON, P.H. & MATSUBARA, M. 2021 Flow visualization and skin friction determination in transitional channel flow. *Exp. Fluids* **62** (2), 1–16.
- YU, X. & LIU, J.T.C. 1991 The secondary instability in Görtler flow. *Phys. Fluids A: Fluid Dyn.* **3** (8), 1845–1847.
- ZANOUN, E.S., NAGIB, H. & DURST, F. 2009 Refined c_f relation for turbulent channels and consequences for high-re experiments. *Fluid Dyn. Res.* **41** (2), 021405.
- ZARIPPOV, D., LI, R., LUKYANOV, A., SKRYPNIK, A., IVASHCHENKO, E., MULLYADZHANOV, R. & MARKOVICH, D. 2023 Backflow phenomenon in converging and diverging channels. *Exp. Fluids* **64** (1), 9.